nature nanotechnology

Article

https://doi.org/10.1038/s41565-022-01249-3

Selective targeting of visceral adiposity by polycation nanomedicine

Received: 27 September 2021

Accepted: 3 October 2022

Published online: 01 December 2022

Check for updates

Qianfen Wan[1,8], Baoding Huang[2,3,8], Tianyu Li[3], Yang Xiao[3], Ying He[1], Wen Du[4], Branden Z. Wang[1], Gregory F. Dakin[5], Michael Rosenbaum[4,6], Marcus D. Goncalves[7], Shuibing Chen[5], Kam W. Leong[3] ✉ & Li Qiang[1] ✉

Obesity is a pandemic health problem with poor solutions, especially for targeted treatment. Here we develop a polycation-based nanomedicine polyamidoamine generation 3 (P-G3) that—when delivered intraperitoneally—selectively targets visceral fat due to its high charge density. Moreover, P-G3 treatment of obese mice inhibits visceral adiposity, increases energy expenditure, prevents obesity and alleviates the associated metabolic dysfunctions. In vitro adipogenesis models and single-cell RNA sequencing revealed that P-G3 uncouples adipocyte lipid synthesis and storage from adipocyte development to create adipocytes that possess normal functions but are deficient in hypertrophic growth, at least through synergistically modulating nutrient-sensing signalling pathways. The visceral fat distribution of P-G3 is enhanced by modifying P-G3 with cholesterol to form lipophilic nanoparticles, which is effective in treating obesity. Our study highlights a strategy to target visceral adiposity and suggests that cationic nanomaterials could be exploited for treating metabolic diseases.

Obesity and being overweight are surging global health challenges, inflicting severe comorbidities including diabetes and cardiovascular diseases to account for the second most preventable death[1]. Obesity is directly caused by the expansion of white adipose tissue (WAT), owing to the formation and growth of adipocytes. Adipocytes function by storing lipids in the form of triglycerides (TGs). The size of an adipocyte can grow up to 20-fold in diameter, theoretically holding ~8,000-fold more lipids[2]. Of note, the metabolic risks of obesity largely depend on body fat distribution rather than excess weight per se. WAT can be mainly classified as subcutaneous or visceral fat according to the anatomical location[3]. The former is underneath the skin, whereas the latter localizes inside the peritoneal cavity and is more robustly associated with obesity comorbidities[4]. Nevertheless, obesity treatment remains an unprecedented challenge, particularly for visceral adiposity.

Cationic nanomaterials, represented by polyamidoamine (PAMAM) dendrimers, have shown promising potential in treating various inflammatory diseases and cancers through neutralizing negatively charged pathogens[5–8] but have never been applied to obesity. During the progression of obesity, the expansion of WAT is accompanied by an increased production of extracellular matrix (ECM)[9], which contains glycosaminoglycans, the known biomacromolecules with the strongest negative charge[10]. The anionic nature of ECM in adipose tissue suggests that cationic nanomaterial would be enriched in this tissue. P-G3 is the third-generation PAMAM dendrimer with 32 surface amine groups (molecular weight (MW), 6,909 g mol^{-1}; size, 36 Å)[11]. Here we report that P-G3 and its lipophilic derivative are preferentially distributed to visceral fat and inhibit diet-induced obesity (DIO) in a murine model, enlightening a polycationic strategy to tackle visceral adiposity.

[1]Naomi Berrie Diabetes Center and Department of Pathology and Cell Biology, Columbia University, New York, NY, USA. [2]Department of Orthopaedic Surgery, The Sixth Affiliated Hospital, Sun Yat-Sen University and Guangdong Provincial Key Laboratory of Orthopaedics and Traumatology, Guangzhou, China. [3]Department of Biomedical Engineering, Columbia University, New York, NY, USA. [4]Department of Medicine, Columbia University, New York, NY, USA. [5]Department of Surgery, Weill Cornell Medicine, New York, NY, USA. [6]Department of Pediatrics, Columbia University, New York, NY, USA. [7]Department of Medicine, Weill Cornell Medicine, New York, NY, USA. [8]These authors contributed equally: Qianfen Wan, Baoding Huang. ✉e-mail: kam.leong@columbia.edu; lq2123@cumc.columbia.edu

P-G3 is selectively distributed to visceral fat

Leveraging the highly anionic ECM in adipose tissue, we tested whether P-G3 can bind to adipose tissue (Fig. 1a and Extended Data Fig. 1a). Isolated ECM from visceral epididymal white adipose tissue (eWAT) and subcutaneous inguinal white adipose tissue (iWAT) showed strong absorption of Cy5-fluorescent-labelled P-G3. Further, the ex vivo incubation of P-G3 with intact organs showed a much stronger fluorescent signal in iWAT and eWAT than in non-adipose tissues, without detection in the attached testis (Fig. 1a). These data imply a preferential biodistribution of P-G3 into WAT.

In DIO mice, Cy5-P-G3 signals were enriched in the peritoneal region and peaked at 24 h post-injection via the regular intraperitoneal (i.p.) delivery route (Fig. 1b,c). At the organ level, the strongest fluorescent signals were detected in all the visceral fat depots, including eWAT, mesenteric white adipose tissue (mWAT) and retroperitoneal white adipose tissue (rWAT), in striking contrast to the minimal signals in iWAT and interscapular brown adipose tissue (BAT) (Fig. 1d and Extended Data Fig. 1b). Low levels of Cy5 signal were detected in the liver, lung, spleen and kidney, indicating that P-G3 entered circulation and was absorbed by other tissues (Fig. 1d and Extended Data Fig. 1b). Histological analyses of tissue sections confirmed the more robust signal in eWAT but not in iWAT and liver (Fig. 1e). Importantly, the P-G3 Cy5 signal evenly penetrated into eWAT rather than attached to the tissue surface. Moreover, the colocalization of P-G3 Cy5 signal and adipocyte marker caveolin-1 was detected (Fig. 1f), confirming entry into adipocytes. This tissue distribution pattern was recapitulated in chow-fed lean mice (Extended Data Fig. 1c–e). No signal was detected in any adipose tissue by intravenous injection, but subcutaneous fat injection locally retained the signal without distributing into visceral fat despite marginal deposition into other organs (Extended Data Fig. 1f), denoting a diet-independent and delivery-route-dependent visceral fat distribution of P-G3.

To understand this visceral fat distribution of P-G3, we manipulated cationic polymers regarding charge and structure by employing branched polyethylenimine (B-PEI) (MW, 25,000 g mol^{-1}) and linear polyethylenimine (L-PEI) (MW, 2,500 g mol^{-1}; weaker cationic charges) (Fig. 1g). Compared with P-G3, B-PEI showed similar preferential distribution to visceral fat depots, whereas L-PEI still displayed overall fainter but still visceral fat preference (Fig. 1h and Extended Data Fig. 1b). Furthermore, polyanionic PAMAM G2.5 (P-G2.5), which has the same structure as P-G3 but is sodium carboxylate terminated (Fig. 1g), showed no signal in any of the tissues (Fig. 1i). These data together indicate that a cationic character is essential for selective visceral fat distribution, and the selectivity can be further tuned by charge density and molecular structure.

P-G3 inhibits DIO

Administering P-G3 nearly completely flattened the steep weight gain on high-fat-diet (HFD) feeding, resulting in 20% less body weight after six-week treatment (Fig. 2a–c). This anti-obesity effect was not caused by reducing food intake (Fig. 2d), intestinal absorption (Fig. 2e) or lean mass (Fig. 2f). Instead, it was exclusively accounted for by inhibiting fat mass (Fig. 2f). This inhibition was more pronounced on the eWAT than on the iWAT, reduced by 70% and 50%, respectively (Fig. 2g). The inhibition of weight gain was recapitulated in female mice (Extended Data Fig. 2a–d) but blunted in chow-fed lean mice (Extended Data Fig. 2e–g), reinforcing the anti-obesity effect of P-G3.

Adipocyte hypertrophy was restrained by P-G3 treatment in both eWAT and iWAT (Fig. 2h,i), underlying their reduced depot sizes (Fig. 2g). Consistently, the expression of adipocyte markers in eWAT, including key adipogenic regulators (*Cebpb*, *Pparg1*, *Pparg2* and *Cebpa*) and pan-adipocyte markers (*Fabp4*, *Adipoq*, *Plin1*, *Cd36* and *Lep*) were dramatically suppressed (Fig. 2j and Extended Data Fig. 3a). This extent of repression of adipocyte genes is not typical in regular obesity-resistant models but similar to mice lacking adipose tissue, namely, lipoatrophy[12,13]. Lipoatrophy is associated with adipose tissue inflammation, insulin resistance, dyslipidemia and liver steatosis. However, P-G3-treated mice showed comparable levels of glucose, insulin, non-esterified fatty acid (NEFA) and TG with the control mice (Extended Data Fig. 3b–e). They did not develop hepatic steatosis but rather showed repressed expression of gluconeogenic (*Foxo1* and *G6pc*) and lipogenic (*Pklr* and *Scd1*) genes with normal glycogen storage (Extended Data Fig. 3f,g), suggesting uncompromised or even improved liver metabolic health. Moreover, plasma alanine aminotransferase, the liver injury marker, was not increased in P-G3-treated mice (Extended Data Fig. 3h). Interestingly, macrophage marker F4/80 was increased in the eWAT of P-G3-treated mice but without inducing inflammatory genes *Tnfa* and *Il6* (Extended Data Fig. 3i,j). Instead, the anti-inflammatory M2 macrophage markers *Il10*, *Cd206* and *Arg1* were upregulated, further supporting the healthy remodelling of visceral fat by P-G3. Despite the similar inhibition of adipocyte hypertrophy in iWAT (Fig. 2i), its gene expression was in striking contrast to eWAT, with the largely normal expression of adipocyte genes (Fig. 2k). Therefore, the global repression of adipocyte genes in eWAT probably arises from the direct impact of P-G3, whereas the relatively normal adipocyte gene expression pattern in iWAT is secondary to the lean phenotype, coinciding with its biodistribution to visceral fat.

An indirect calorimetric analysis of energy homoeostasis revealed that P-G3 treatment increased heat production and O_2 consumption (Fig. 2l,m) without affecting locomotor activity, respiratory exchange ratio and food intake (Extended Data Fig. 3k–m). Furthermore, the obesity-associated metabolic dysfunctions, specifically glucose intolerance and insulin resistance, were alleviated (Fig. 2n,o). The downstream target of insulin signalling—GSK3β phosphorylation—was consistently increased in the eWAT of P-G3-treated mice (Extended Data Fig. 3a). Moreover, P-G3 treatment did not affect lipid absorption and homoeostasis (Extended Data Fig. 3n) or lipolysis (Extended Data Fig. 3o,p). Overall, P-G3 treatment increases energy expenditure to underlie its inhibition of obesity, which leads to improved metabolic consequences.

P-G3 impedes adipocyte hypertrophic growth

The profound fat-remodelling function of P-G3 prompted us to test any direct effect of P-G3 on adipocyte development by employing a classic in vitro adipogenesis model—3T3-L1 cells—that can be differentiated into lipid-containing adipocytes through the hormonal induction of adipogenic genes and lipid synthesis genes[14]. Less lipid accumulation was observed in P-G3-treated cells; however, there were

Fig. 1 | P-G3 is selectively distributed to visceral fat. a, Schematic of the P-G3 structure and adipose tissue with ECM and ex vivo imaging of Cy5 fluorescent signal of tissues after incubating with Cy5-labelled P-G3 for 45 min. All the tissues were imaged at the same exposure. **b**, Schematic of P-G3 administration and tissue distribution. The colour of the outer ring represents distribution preference (created with BioRender.com). **c**, In vivo imaging of P-G3 signal at 8, 24 and 48 h post i.p. injection. PBS-treated (vehicle) mice were used as the basal reference. **d**, Imaging of signal intensity in individual tissues from mice sacrificed at 80 h post-injection. **e**, Confocal microscopy analysis of P-G3 distribution in eWAT, iWAT and liver from mice at 80 h after Cy5-labelled P-G3 (red colour) injection. **f**, Colocalization of Cy5-labelled P-G3 with DAPI (staining for nuclei, blue colour) and caveolin-1 (staining for adipocyte cell membrane, green colour) in eWAT. Representative data in **e** and **f** were independently repeated twice with similar results. **g**, Structural illustrations of P-G3, branched polyethylenimine (B-PEI), linear polyethylenimine (L-PEI) and polyanionic P-G2.5. **h**,**i**, Tissue distribution of Cy5-labelled P-G3, B-PEI and L-PEI (**h**) and P-G2.5 (**i**) at 72 h post-injection. The same tissues were used for the PBS and P-G3 groups. The unit of the fluorescent scale bar is photons s^{-1} cm^{-2} sr^{-1}. Panel **a** is adapted with permission from ref. [37] (5W Graphics/Columbia Engineering).

https://doi.org/10.1038/s41565-022-01249-3

more lipid-positive cells but with smaller droplet sizes (Fig. 3a). In a parallel C3H10T1/2 model, we observed faster lipid accumulation in early adipogenesis (day 4) but similarly smaller lipid droplets after full differentiation (since day 6) (Fig. 3b and Extended Data Fig. 3a). Consistently, there was an overall earlier induction of key adipogenic factors by day 4 of differentiation in P-G3-treated 3T3-L1 cells, including *Cebpb*, *Pparg1*, *Pparg2* and *Cebpa*, as well as pan-adipocyte markers (*Fabp4*, *Cfd* and *Adipoq*) (Fig. 3c); however, all these mature adipocyte

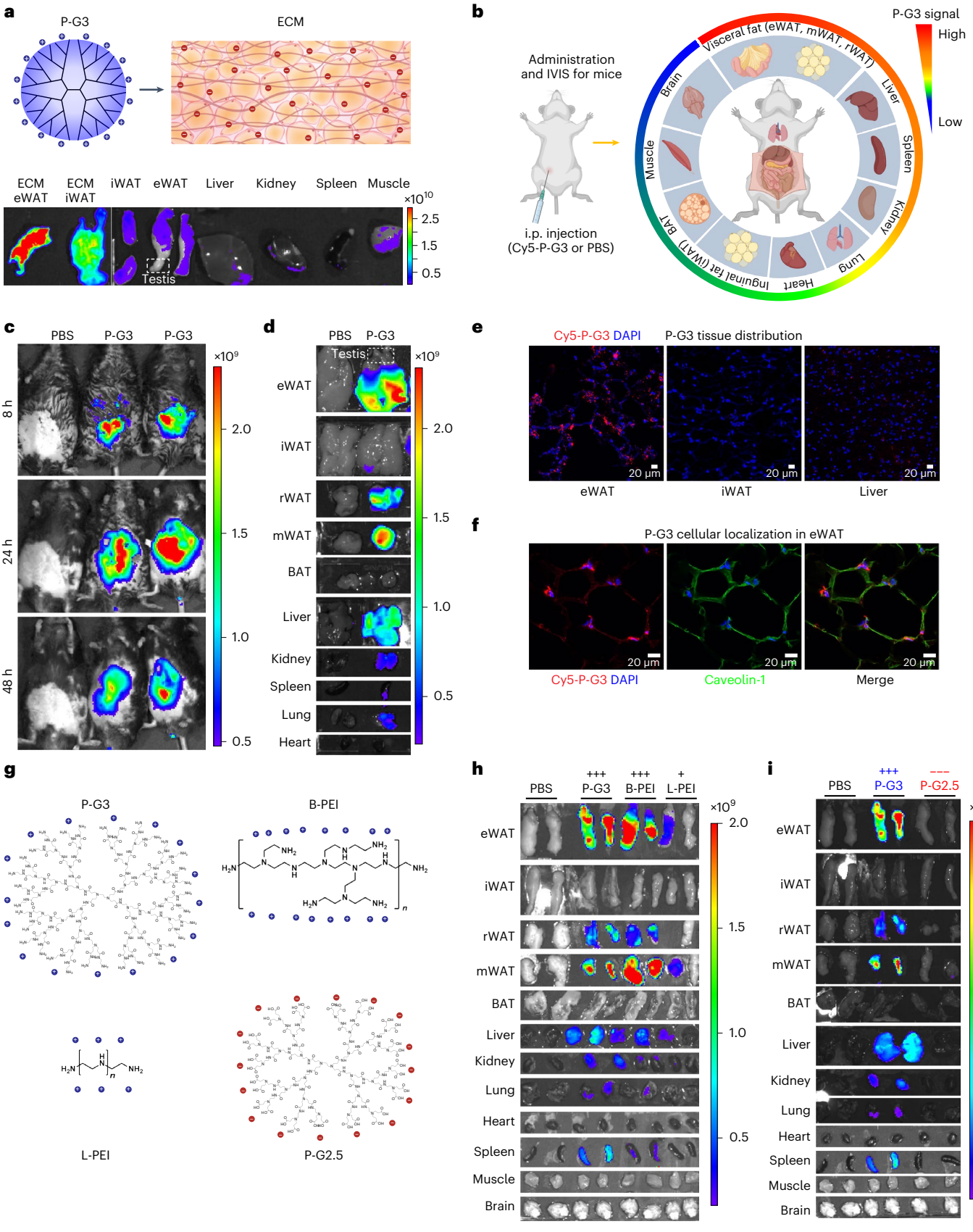

https://doi.org/10.1038/s41565-022-01249-3

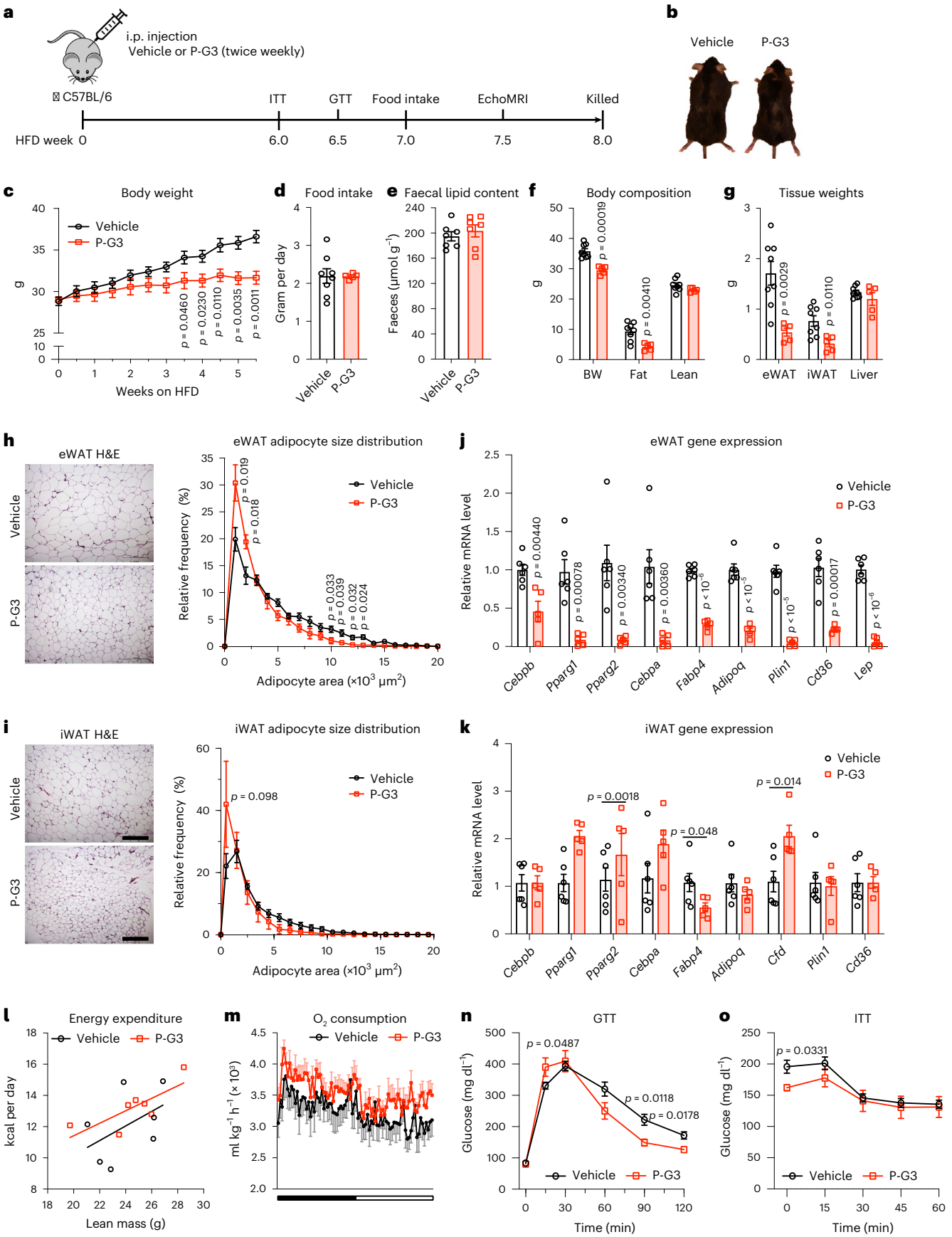

genes were repressed in the following stage of hypertrophic growth (Extended Data Fig. 4b), probably owing to the less lipid accumulation to sustain their maturation and phenocopying the overwhelmed repression in eWAT (Fig. 2j). This is particularly true for *Plin1*, a gene encoding a lipid-droplet-coating protein Perilipin 1. It was normally induced during early adipogenesis but halted after day 4 and markedly

https://doi.org/10.1038/s41565-022-01249-3

Fig. 2 | P-G3 prevents DIO and improves metabolic health. a, Schematic of the experimental design (created with BioRender.com). **b**, Representative mouse pictures at sacrifice after eight-week treatment. **c**, Body weight curve before disturbance by metabolic measurements. **d**, Average food intake of five continuous days on HFD feeding. **e**, Faecal free fatty acid content (separate cohort of mice, $n = 7$ versus 7). **f**, Body composition determined by EchoMRI. **g**, Tissue weights at sacrifice. **h**–**k**, Histological analysis (H&E staining) and adipocyte size distribution and gene expression of eWAT (**h** and **j**) and iWAT (**i** and **k**). **l**,**m**, Male mice received three dosages of P-G3 (10 mg per kg of body weight) or vehicle (i.p.) twice weekly since the beginning of HFD feeding and then housed singly in metabolic cages for calorimetric analysis ($n = 7$ versus 7). Energy expenditure indicated by correlating heat production to lean body mass (**l**). O_2 consumption (**m**). **n**,**o**, GTT (**n**) and ITT (**o**) in mice at 6.5 and 6.0 weeks of P-G3 treatment (same cohort as in **a**). For **c**, **d**, **f**–**i**, **n** and **o**, data are presented as mean ± s.e.m. ($n = 8$ for vehicle group; $n = 5$ for P-G3 group). For **j** and **k**, data are presented as mean ± s.e.m. ($n = 6$ for vehicle group; $n = 5$ for P-G3 group). For **e**, **l** and **m**, data are presented as mean ± s.e.m. ($n = 7$ for vehicle group; $n = 7$ for P-G3 group). Statistical significance is calculated via a two-tailed Student's *t*-test.

dropped in late differentiation by P-G3 treatment (Extended Data Fig. 4b), in direct correlation with impaired lipid accumulation. In summary, P-G3 accelerates the adipocyte development program but inhibits hypertrophic growth.

The defining function of fat cells is to store lipids, which is essentially supported by the activation of genes for lipid synthesis. However, the inductions of the key lipogenic factors *Fasn*, *Scd1*, *Srebf1*, *Acaca*, *Acacb* and glyceroneogenic gene *Pck1* were blunted by P-G3 treatment during 3T3-L1 cell differentiation (Fig. 3d). This phenomenon was reproduced in human primary adipocytes (Extended Data Fig. 4c), with a more potent inhibition of lipogenic genes in the later stage (Extended Data Fig. 4d). Thus, P-G3 uncouples lipid synthesis from adipogenesis—two innately conjugated processes in adipocyte development—to create 'dwarf' adipocytes, denoting normal adipocyte functions but deficient in lipid synthesis (Fig. 3e). This uncoupling also holds true in mature 3T3-L1 (Fig. 3f) and C3H10T1/2 (Extended Data Fig. 4e) adipocytes with transient P-G3 treatment. Moreover, the key TG synthesis genes *Gpat3*, *Lipin1* and *Dgat2* were also significantly repressed (Fig. 3f). This prevailing inhibition of the lipid synthesis program by P-G3 was recapitulated in vivo in eWAT (Fig. 3g) but not in iWAT (Extended Data Fig. 4f). Importantly, the ex vivo treatment of human omental fat with P-G3 led to a strong repression of key lipogenic genes in contrast to an upregulation of adipogenic genes *CEBPB* and *FABP4* and blunted effects on *PPARG1* and *PPARG2* (Fig. 3h), indicating that P-G3's effects are translatable in human visceral fat.

Of note, acute three-day P-G3 treatment primarily repressed lipid synthesis genes without affecting pan-adipocyte markers in eWAT (Extended Data Fig. 4g,h), implying that the downregulation of adipocyte genes is secondary to mitigated lipid storage in chronic treatment. To further demonstrate an independent regulation of lipid synthesis from adipogenesis, we employed a PPARγ-overexpressing cell line to bypass the endogenous adipogenic cascade[15]. Again, P-G3 reduced their lipid droplet size (Extended Data Fig. 4i), reinforcing the uncoupling of lipid synthesis from adipogenesis. In addition, this uncoupling requires fine-tuning the charge and structure since B-PEI, unlike P-G3, showed toxicity to adipocytes in vitro (Extended Data Fig. 4j).

P-G3 dulls nutrient-sensing signals in adipocyte development

To understand P-G3's bifurcate regulation of adipocyte development, we performed single-cell RNA sequencing (scRNA-seq) during 3T3-L1 cell differentiation. The heterogeneity and dynamics of adipogenesis were resolved at the single-cell level for the first time (to the best of our knowledge), clustered as preadipocytes, immature adipocytes, adipocytes and lipogenic adipocytes (Fig. 4a,b, and Extended Data Fig. 5a). Consistent with its proadipogenic function (Fig. 3c), P-G3 accelerated early adipogenesis at day 3 of differentiation, indicated by a higher adipocyte proportion (10.17% versus 7.68% in control) (Fig. 4c,d, and Supplementary Table 1). However, despite their faster adipogenesis, P-G3-treated cells were reluctant to progress into the mature stage, with a population of 8.70% lipogenic cells on day 6, compared with 13.85% in the control cells. The upregulation of adipocyte genes and downregulation of lipid-related genes by P-G3 treatment were ultimately resolved at the single-cell level (Extended Data Fig. 5b), buttressing the 'dwarf' adipocyte phenotype.

Next, we identified the driver genes in altered adipocyte development using RNA velocity and regulon analyses (Extended Data Fig. 5c,d)[16–18]. Notably, the gene expression pattern was different from RNA velocities, dynamic rates of mRNA synthesis, splicing and degradation (Fig. 4e–h). For example, the mRNA expression of *Pparg*, the master adipogenic factor, was high in mature adipocytes (Fig. 4e), but its unspliced/spliced mRNA velocity was stimulated in premature adipocytes (Fig. 4f). Similar patterns were observed in the key lipogenic gene *Fasn* (Fig. 4g,h) and other representative adipogenic genes (Extended Data Fig. 5e), suggesting that the active regulations of these genes are initiated before reaching their full expression. Furthermore, QIAGEN ingenuity pathway analysis (IPA) software identified the altered pathways in lipogenesis and adipogenesis. P-G3 prompts oxidative phosphorylation, PPAR and PPARα/RXRα signalling but downregulates pathways in nutrient sensing, mTOR, nicotinamide adenine dinucleotide (NAD), sirtuin signalling and inflammation (Fig. 4i). Our study, thus, provides a framework of single-cell analysis assessing the cellular heterogeneity and changes on P-G3 treatment.

To determine the functioning size of P-G3 to affect adipocyte development, we conjugated P-G3 to carboxylate microbeads to attach to the cell surface but block its entry into the cell; however, adipogenesis was impaired (Extended Data Fig. 6a,b). It is possible that P-G3 changes the extracellular environment to affect adipocytes. We, therefore, incubated the P-G3 beads in the transwell to prevent their contact with adipocytes but observed minimal effect on adipocyte differentiation (Extended Data Fig. 6a,b). Hence, the uncoupling effects of P-G3 on adipocytes require its entry into the cells. Cationic materials are known to enter cells mainly through endocytosis[19–21]. We detected the colocalization of P-G3 with early endosomes in C3H10T1/2 adipocytes at 1 h of treatment following the earlier colocalization with the plasma membrane at 15 min (Extended Data Fig. 6c). Over

Fig. 3 | P-G3 uncouples lipid synthesis from adipocyte formation. a–**d**, 3T3-L1 or C3H10T1/2 preadipocytes were differentiated in the presence of 10 μg ml^{-1} P-G3. Oil Red O staining of lipid droplets in 3T3-L1 cells on day 6 of differentiation (**a**). BODIPY staining of lipid droplets and the quantification of lipid droplet size in C3H10T1/2 cells on differentiation day 12 (**b**). The representative data in **a** and **b** were independently repeated three times with similar results. **c**,**d**, qPCR analysis of the gene expression of adipogenic markers (**c**) and lipogenic genes (**d**) during the time course of 3T3-L1 differentiation with or without P-G3 treatment. The data are represented as mean ± s.e.m. ($n = 4, 4$). Statistical significance is calculated via a two-tailed Student's *t*-test. **e**, Schematic of the P-G3's bifurcate regulation of adipocyte development (created with BioRender.com). **f**, qPCR analysis of gene expression in mature 3T3-L1 adipocytes after treatment with 10 μg ml^{-1} P-G3 from day 9 to day 14. The data are represented as mean ± s.e.m. ($n = 4, 4$). Statistical significance is calculated via a two-tailed Student's *t*-test. **g**, qPCR analysis of expression of the genes involved in lipid metabolism in eWAT from HFD mice after eight-week P-G3 treatment. The data are represented as mean ± s.e.m. ($n = 6, 5$). Statistical significance is calculated via a two-tailed Student's *t*-test. **h**, qPCR analysis of expression in ex vivo human omental adipose tissue after treatment with 10 μg ml^{-1} P-G3 for eight days. The data are represented as mean ± s.e.m. ($n = 4, 3$). Statistical significance is calculated via a two-tailed Student's *t*-test.

https://doi.org/10.1038/s41565-022-01249-3

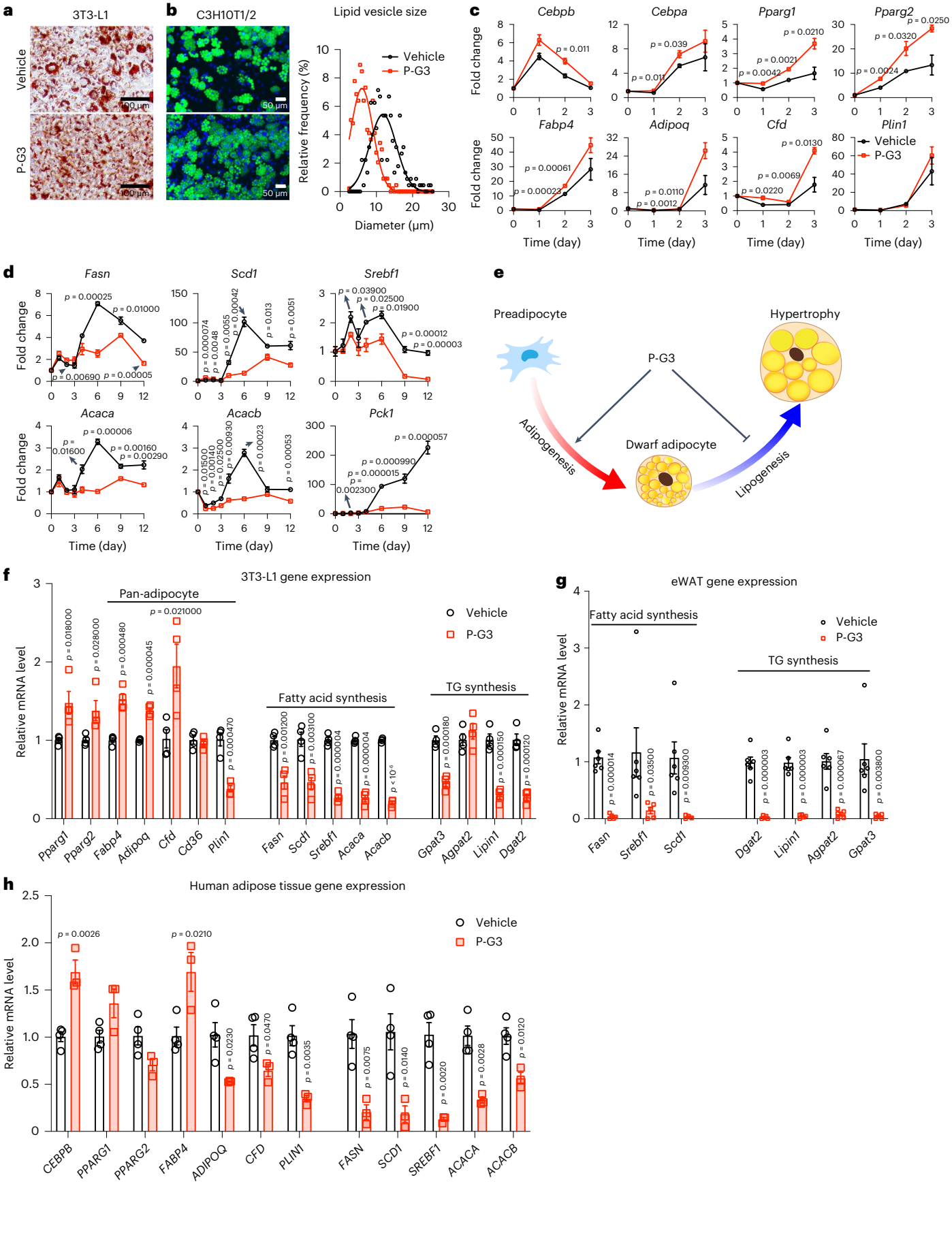

https://doi.org/10.1038/s41565-022-01249-3

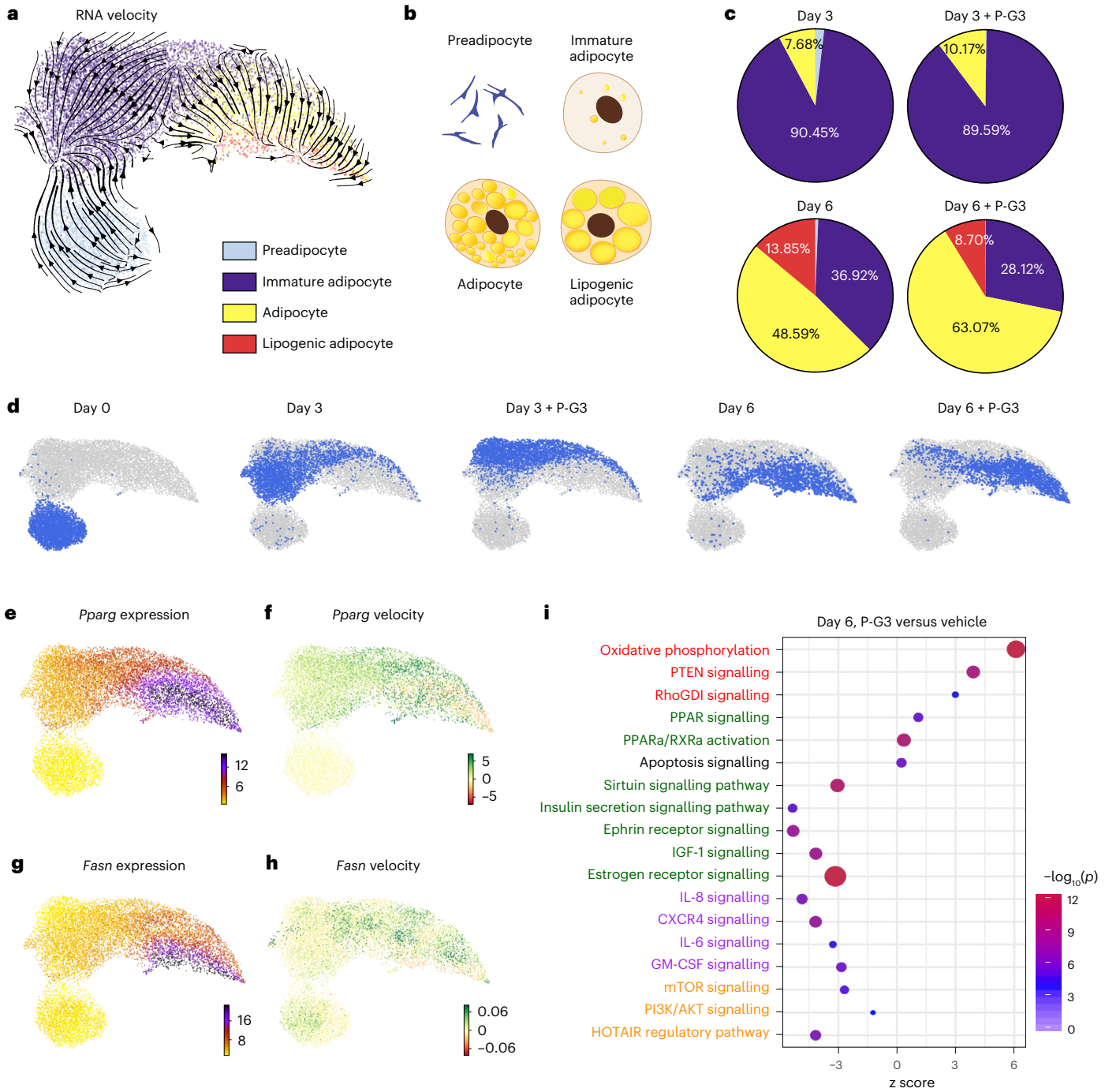

Fig. 4 | scRNA-seq analyses reveal the bifurcate regulation of adipocyte development by P-G3. a, RNA velocity revealed the cell dynamics during 3T3-L1 differentiation. **b**, Schematic of the heterogeneity of adipogenesis, including preadipocyte, immature adipocyte, adipocyte and lipogenic adipocyte. **c**, Cell-type composition of the cells on day 3 and day 6 of differentiation. **d**, Clustering of adipocytes shown in the uniform manifold approximation and projection space coloured at different time points during adipogenesis with or without P-G3 treatment. **e**, Expression of spliced mature mRNA of *Pparg* gene. **f**, RNA velocity of *Pparg* gene based on unspliced/spliced mRNA ratio. **g**, Expression of spliced mature mRNA of *Fasn* gene showed the cell population as lipogenic adipocytes. **h**, RNA velocity of *Fasn* gene based on unspliced/spliced mRNA ratio. **i**, Dot plot showing the key altered pathways on day 6 by QIAGEN IPA two-sided analysis. The dot sizes and colour reflect the *p* values (shown in −log10(*p* value)) in each pathway.

time, the accumulation of P-G3 was observed in lysosomes, whereas only weak colocalization was detected in the endoplasmic reticulum, mitochondria or lipid droplets (Fig. 5a and Extended Data Fig. 6d). It is plausible that the cationic P-G3 may inhibit the acidification of lysosomes to interfere with the latter's function. Indeed, P-G3 treatment in 3T3-L1 adipocytes decreased lysosomal activity ~10-fold, mimicking the lysosome inhibitor bafilomycin A1 (Fig. 5b and Extended Data Fig. 6e).

The scRNA-seq analysis revealed the downregulation of the mTOR pathway, which is critical for lipid synthesis in adipocytes[22]. Here mTOR localizes on the lysosome and its activity depends on the acidification of the lysosome[23]. We, therefore, asked whether P-G3 represses the mTOR pathway in adipocytes. P-G3 suppressed the mTOR activation as indicated by its decreased phosphorylation and that of downstream substrates S6K and 4E-BP1 during adipogenesis (Fig. 5c). The inhibition

of mTOR signalling by P-G3 was potentiated in eWAT along with a strong inhibition of fatty acid synthase (FASN) (Fig. 5d). Moreover, treating 3T3-L1 (Fig. 5e) and C3H10T1/2 (Extended Data Fig. 6f) adipocytes with rapamycin, an mTOR inhibitor, largely mimicked P-G3's inhibition of the lipid synthesis genes (Fig. 5e). Of note, compared with rapamycin, the inhibition by P-G3 is more prevailing with additional repression of *Fasn*, *Scd1*, *Pck1* and *Gpat3* (Fig. 5e). These data demonstrate that P-G3 can impair lysosome function and inhibit mTOR activity in adipocytes, partially explaining the repression of lipogenesis.

Regarding the promotion of early adipogenesis by P-G3, scRNA-seq analyses revealed repression on the NAD signalling pathway and sirtuin signalling pathway (Fig. 4i), the latter of which is NAD^+ dependent. NAD is a critical metabolite in regulating various cellular functions such as energy metabolism and differentiation[24]. A precipitous decrease in NAD^+ is required for adipocyte progenitors entering adipogenesis[25]. Indeed, P-G3 efficiently decreased cellular NAD^+ levels in preadipocytes, whereas there was no decrease in mature adipocytes (Fig. 5f and Extended Data Fig. 6g). We then reasoned that if P-G3 prompts early adipogenesis by decreasing the NAD^+ levels, this effect should be abolished by retaining NAD^+. Supplementing the NAD precursor nicotinamide mononucleotide (NMN) during the early adipogenesis stage to boost the intracellular NAD^+ levels counteracted the proadipogenic effect of P-G3 (Fig. 5g). Therefore, P-G3 functions through a synergetic mechanism, probably involving repressed NAD and mTOR signalling, to dissociate lipogenesis from adipogenesis.

Lipophilic P-G3 nanoparticles improve visceral fat targeting

To further improve the visceral fat distribution of P-G3 and reduce the risk of being off-target in other tissues, we covalently attached a lipophilic chain of five constitutive cholesterol molecules to P-G3 (Fig. 6a and Extended Data Fig. 7a). The resulting P-G3-Chol(5) could self-assemble in water to form spherical nanoparticles (NPs; size, 125.0 ± 10.5 nm) and maintain a cationic surface (zeta potential, 56.4 ± 1.1 mV) (Fig. 6b). P-G3-Chol(5) NPs showed the same endocytic uptake pattern by adipocytes as unmodified P-G3 (Extended Data Fig. 7b) and similarly promoted adipogenesis (Extended Data Fig. 7c). More importantly, the NPs displayed a comparable or slightly higher distribution to visceral fat depots as P-G3, but its distributions to the liver, kidney and lung were significantly lower (Fig. 6c and Extended Data Fig. 7d), without affecting the penetration into visceral fat (Extended Data Fig. 7e).

Encouraged by the improved visceral fat specificity of NPs, we tested whether it can offer a therapeutic option in treating visceral obesity (Fig. 6d). In DIO mice with established obesity, a four-week treatment resulted in a leaner phenotype (Fig. 6e) with a 15% decrease in body weight on continuous HFD feeding (Fig. 6f). The lean phenotype was exclusively attributed to a 45% reduction in fat mass, as determined by EchoMRI (Fig. 6g). Consistently, the eWAT depot size was reduced by ~50%, with less reduction in iWAT (Fig. 6h). The adipocyte hypertrophy in obese eWAT was rectified by NPs treatment (Fig. 6i), which was supported by a prevalent suppression of adipogenic regulators, pan-adipocyte markers and lipid biosynthesis genes in the existing mature adipocytes in eWAT (Fig. 6j,k), accompanied by the upregulation of anti-inflammatory M2 macrophage markers (Extended Data Fig. 7f). In line with P-G3's inhibition of lipid synthesis but unaffected lipolysis, NP-treated mice regained less fat during re-feeding rather than losing more fat mass during fasting (Extended Data Fig. 7g). As expected, NP-treated mice showed improved glucose tolerance (Fig. 6l). Again, the mTOR signalling pathway was inhibited in NP-treated eWAT (Extended Data Fig. 7h). Collectively, P-G3-Chol(5) NPs show promising therapeutic potential in treating visceral obesity in DIO mice.

Conclusions

Here we demonstrate that the polycation P-G3 is selectively distributed to visceral fat via the i.p. delivery route to inhibit visceral adiposity and prevent obesity by uncoupling lipid synthesis from adipocyte development, creating 'dwarf' adipocytes. Engineering P-G3 into lipophilic NPs further improves its visceral-fat-selective biodistribution and shows therapeutic potential to treat obesity. More importantly, P-G3 and its NPs derivative overcome the critical barrier to tackling visceral obesity. Unlike subcutaneous fat with multiple available approaches[26], there is no option for visceral adiposity, except for surgical removal developed in rodents and baboons, regardless of the risk and complexity[4,27]. Therefore, our study presents a revolutionary cationic strategy for treating obesity, distinct from the existing anti-obesity interventions.

P-G3 renders adipocytes smaller, either from *de novo* adipocyte formation or in mature adipocytes. In contrast to hypertrophic ones, smaller adipocytes are usually metabolically healthier[28–30], underlying the metabolic improvements by P-G3 treatment. These 'dwarf' adipocytes arise from the prevalent and selective inhibition of lipid synthesis genes. Hence, lipid storage does not necessarily coincide with adipocyte phenotypic development, and P-G3 can uncouple them. The divergent regulation of adipocytes by P-G3 differs from conventional adipocyte manipulations, such as adipocyte delipidation induced by nutrient deprivation or inflammatory reagents to cause the repression of pan-adipocyte genes and loss of adipocyte identity[31–34], or adipocyte browning involving the activation of the thermogenic program without shutting down lipid synthesis. This unique effect of P-G3 is probably mediated through repressing mTOR and NAD^+ signalling—two pivotal metabolic sensing nexuses. The hyperactivation of mTOR has been reported in obesity and type 2 diabetes mellitus[35], signifying the importance of maintaining appropriate mTOR activity. P-G3 may offer an option to fine-tune the mTOR activity to improve metabolic disease management. It is also plausible that P-G3 would target multiple pathways to account for the metabolic benefits. For example, leptin was markedly repressed in the eWAT by P-G3 treatment (Fig. 2j). It is a key adipokine to regulate food intake and energy expenditure through functioning in the brain[36], raising the possibility that P-G3 may influence the adipose tissue–brain communication to tilt the whole-body energy balance towards expenditure.

Cationic charge correlates with polycation's efficacy but also with toxicity. B-PEI has a relatively high charge density and better visceral-fat-targeting efficiency, whereas its toxicity is obvious in vitro. P-G3 is probably at the sweet spot between efficacy and safety, which

Fig. 5 | P-G3 represses mTOR signalling pathway and decreases NAD^+ levels in adipocyte development. a, Colocalization of Cy5-labelled P-G3 (green colour) with DAPI (blue colour) and LysoTracker (red colour) in 3T3-L1 matured adipocytes after 24 h of P-G3 treatment. The representative data are independently repeated twice with similar results. **b**, Flow cytometry determination of lysosomal intracellular activity of C3H10T1/2 cells treated with P-G3 or bafilomycin A1. Cells without self-quenched substrate incubation (grey curve) were used as the baseline reference. **c**, Western blot analysis of the mTOR pathway during 3T3-L1 differentiation in the presence or absence of P-G3. The representative data are independently repeated three times with similar results. **d**, Western blot analysis of the mTOR pathway in the eWAT of P-G3-treated mice and quantification. The data are represented as mean ± s.e.m. ($n = 4, 5$). Statistical significance is calculated via a two-tailed Student's *t*-test. **e**, qPCR analysis of lipogenic genes in 3T3-L1 adipocytes after rapamycin or P-G3 treatment from day 4 to day 6. The data are represented as mean ± s.e.m. ($n = 4, 4$). Statistical significance is calculated via a two-tailed Student's *t*-test (treatment group versus vehicle group). **f**, Decrease in cellular NAD^+ levels in 3T3-L1 preadipocytes after 10 μg ml^{-1} P-G3 treatment for 14 h. The data are represented as mean ± s.e.m. ($n = 3, 3$). Statistical significance is calculated via a two-tailed Student's *t*-test. **g**, Gene expression of 3T3-L1 cells treated with 10 μg ml^{-1} P-G3, or P-G3 (10 μg ml^{-1}) and NMN (20 mM) at day 0–3 during differentiation. The data are represented as mean ± s.e.m. ($n = 4, 4$). Statistical significance is calculated via a two-tailed Student's *t*-test (treatment group versus vehicle group).

https://doi.org/10.1038/s41565-022-01249-3

could be further optimized by cholesterol modification. Moreover, leveraging polycations' carrier capacity in combination with the visceral-fat-specific targeting property demonstrated here, it is highly feasible to encapsulate fat-manipulating agents into P-G3 NPs to specifically deliver them into visceral fat for additive anti-obesity benefit but reduced off-target effects. Collectively, our study highlights a strategy to target visceral adiposity and suggests cationic nanomaterials could be exploited for treating metabolic diseases.

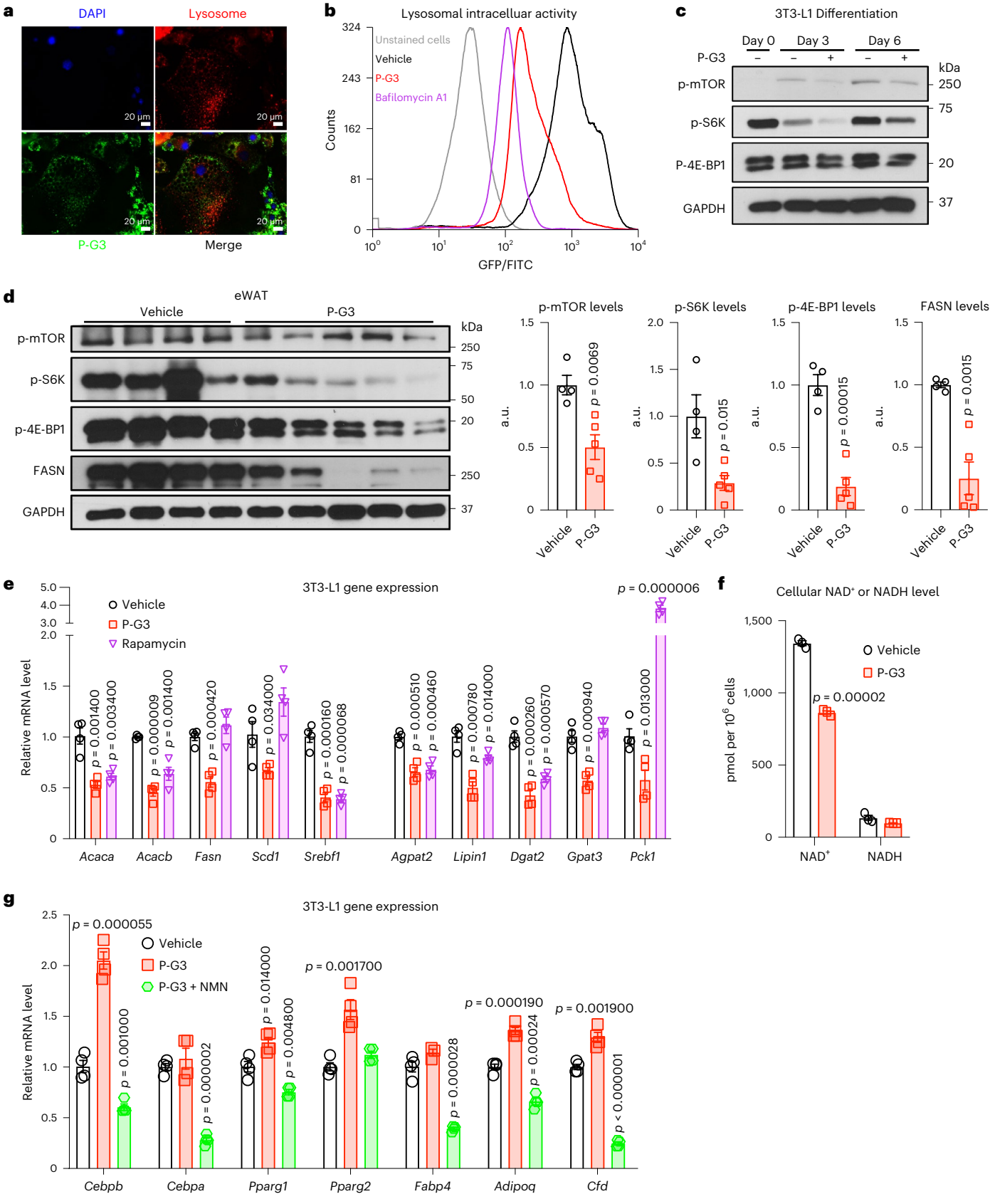

https://doi.org/10.1038/s41565-022-01249-3

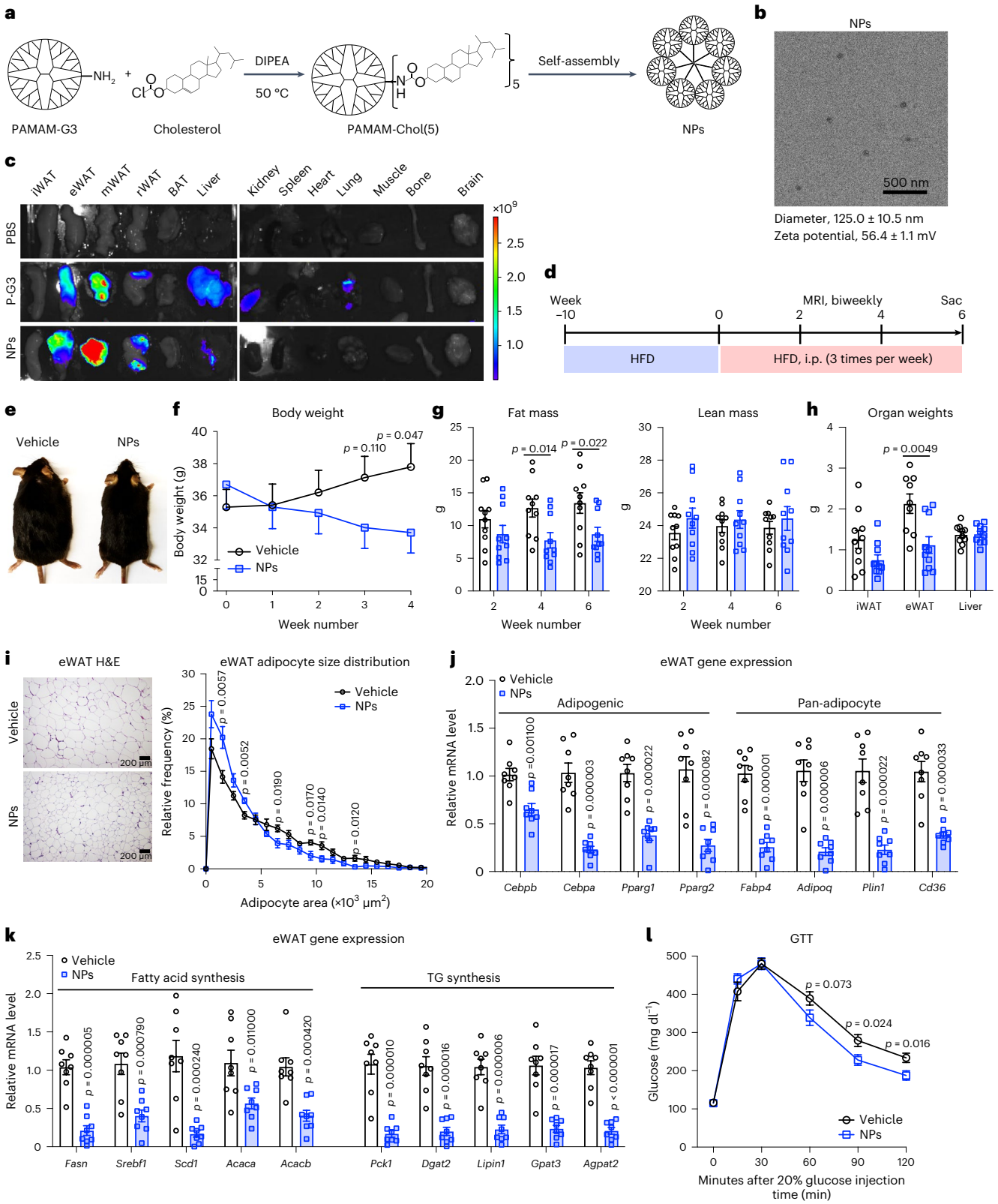

Fig. 6 | Engineering P-G3 to improve visceral fat distribution and treat obesity. a, Structure of adding a 5× cholesterol tail to P-G3 to generate P-G3-Chol(5), which further self-assembles in water and forms spherical NPs. **b**, Electronic microscopy of P-G3-Chol(5) NPs and characterizations. The representative data are independently repeated twice with similar results. **c**, 200 μg Cy5-labelled NPs or Cy5-labelled P-G3 were i.p. injected into mice and IVIS determination of tissue distribution at 72 h post-injection. **d**, Schematic of the experimental design for obesity treatment. **e**, Representative mouse pictures after six weeks of NPs treatment. **f**, Body weight curve before disturbance by metabolic measurements. **g**, Body composition changes during the treatment. **h**, Tissue weights at sacrifice. **i**, Histological analysis (H&E staining) and adipocyte size distribution of eWAT. **j**,**k**, qPCR analysis of gene expression of adipogenic (**j**) and lipogenic (**k**) markers in eWAT after six-week treatment. The data are represented as mean ± s.e.m. ($n = 8, 8$). Statistical significance is calculated via a two-tailed Student's *t*-test. **l**, GTT of mice at 5 weeks post-injection. For **d**–**i** and **l**, $n = 10, 10$, except for **h** eWAT ($n = 9, 10$). The data are represented as mean ± s.e.m. The unit of the fluorescent scale bar is photons $s^{-1}\,cm^{-2}\,sr^{-1}$.

Online content

Any methods, additional references, Nature Portfolio reporting summaries, source data, extended data, supplementary information, acknowledgements, peer review information; details of author contributions and competing interests; and statements of data and code availability are available at https://doi.org/10.1038/s41565-022-01249-3.

References

1. Danaei, G. et al. The preventable causes of death in the United States: comparative risk assessment of dietary, lifestyle, and metabolic risk factors. *PLoS Med.* **6**, e1000058 (2009).
2. Verboven, K. et al. Abdominal subcutaneous and visceral adipocyte size, lipolysis and inflammation relate to insulin resistance in male obese humans. *Sci. Rep.* **8**, 4677 (2018).
3. Kajimura, S., Spiegelman, B. M. & Seale, P. Brown and beige fat: physiological roles beyond heat generation. *Cell Metab.* **22**, 546–559 (2015).
4. Huffman, D. M. & Barzilai, N. Role of visceral adipose tissue in aging. *Biochim. Biophys. Acta* **1790**, 1117–1123 (2009).
5. Svenson, S. & Tomalia, D. A. Dendrimers in biomedical applications—reflections on the field. *Adv. Drug Deliv. Rev.* **57**, 2106–2129 (2005).
6. Lee, J. et al. Nucleic acid-binding polymers as anti-inflammatory agents. *Proc. Natl Acad. Sci. USA* **108**, 14055–14060 (2011).
7. Lee, J. et al. Nucleic acid scavenging microfiber mesh inhibits trauma-induced inflammation and thrombosis. *Biomaterials* **120**, 94–102 (2017).
8. Pisetsky, D. S., Lee, J., Leong, K. W. & Sullenger, B. A. Nucleic acid-binding polymers as anti-inflammatory agents: reducing the danger of nuclear attack. *Expert Rev. Clin. Immunol.* **8**, 1–3 (2012).
9. Mariman, E. C. & Wang, P. Adipocyte extracellular matrix composition, dynamics and role in obesity. *Cell. Mol. Life Sci.* **67**, 1277–1292 (2010).
10. Puri, S., Coulson-Thomas, Y. M., Gesteira, T. F. & Coulson-Thomas, V. J. Distribution and function of glycosaminoglycans and proteoglycans in the development, homeostasis and pathology of the ocular surface. *Front Cell Dev. Biol.* **8**, 731 (2020).
11. Esfand, R. & Tomalia, D. A. Poly(amidoamine) (PAMAM) dendrimers: from biomimicry to drug delivery and biomedical applications. *Drug Disco. Today* **6**, 427–436 (2001).
12. Pajvani, U. B. et al. Fat apoptosis through targeted activation of caspase 8: a new mouse model of inducible and reversible lipoatrophy. *Nat. Med.* **11**, 797–803 (2005).
13. Wang, F., Mullican, S. E., DiSpirito, J. R., Peed, L. C. & Lazar, M. A. Lipoatrophy and severe metabolic disturbance in mice with fat-specific deletion of PPARγ. *Proc. Natl Acad. Sci. USA* **110**, 18656–18661 (2013).
14. Farmer, S. R. Transcriptional control of adipocyte formation. *Cell Metab.* **4**, 263–273 (2006).
15. Li, D. et al. Distinct functions of PPARγ isoforms in regulating adipocyte plasticity. *Biochem. Biophys. Res. Commun.* **481**, 132–138 (2016).
16. La Manno, G. et al. RNA velocity of single cells. *Nature* **560**, 494–498 (2018).
17. Bergen, V., Lange, M., Peidli, S., Wolf, F. A. & Theis, F. J. Generalizing RNA velocity to transient cell states through dynamical modeling. *Nat. Biotechnol.* **38**, 1408–1414 (2020).
18. Aibar, S. et al. SCENIC: single-cell regulatory network inference and clustering. *Nat. Methods* **14**, 1083–1086 (2017).
19. Hwang, M. E., Keswani, R. K. & Pack, D. W. Dependence of PEI and PAMAM gene delivery on clathrin- and caveolin-dependent trafficking pathways. *Pharm. Res.* **32**, 2051–2059 (2015).
20. Fox, L. J., Richardson, R. M. & Briscoe, W. H. PAMAM dendrimer-cell membrane interactions. *Adv. Colloid Interface Sci.* **257**, 1–18 (2018).
21. Kitchens, K. M., Foraker, A. B., Kolhatkar, R. B., Swaan, P. W. & Ghandehari, H. Endocytosis and interaction of poly (amidoamine) dendrimers with Caco-2 cells. *Pharm. Res.* **24**, 2138–2145 (2007).
22. Saxton, R. A. & Sabatini, D. M. mTOR signaling in growth, metabolism, and disease. *Cell* **168**, 960–976 (2017).
23. Chung, C. Y. et al. Covalent targeting of the vacuolar H(+)-ATPase activates autophagy via mTORC1 inhibition. *Nat. Chem. Biol.* **15**, 776–785 (2019).
24. Rajman, L., Chwalek, K. & Sinclair, D. A. Therapeutic potential of NAD-boosting molecules: the in vivo evidence. *Cell Metab.* **27**, 529–547 (2018).
25. Ryu, K. W. et al. Metabolic regulation of transcription through compartmentalized NAD(+) biosynthesis. *Science* **360**, eaan5780 (2018).
26. Zhang, Y. et al. Locally induced adipose tissue browning by microneedle patch for obesity treatment. *ACS Nano* **11**, 9223–9230 (2017).
27. Andrew, M. S. et al. Mesenteric visceral lipectomy using tissue liquefaction technology reverses insulin resistance and causes weight loss in baboons. *Surg. Obes. Relat. Dis.* **14**, 833–841 (2018).
28. Ghaben, A. L. & Scherer, P. E. Adipogenesis and metabolic health. *Nat. Rev. Mol. Cell Biol.* **20**, 242–258 (2019).
29. Tandon, P., Wafer, R. & Minchin, J. E. N. Adipose morphology and metabolic disease. *J. Exp. Biol.* **221**, jeb164970 (2018).
30. Acosta, J. R. et al. Increased fat cell size: a major phenotype of subcutaneous white adipose tissue in non-obese individuals with type 2 diabetes. *Diabetologia* **59**, 560–570 (2016).
31. Brown, J. M. et al. Conjugated linoleic acid induces human adipocyte delipidation: autocrine/paracrine regulation of MEK/ERK signaling by adipocytokines. *J. Biol. Chem.* **279**, 26735–26747 (2004).
32. House, R. L. et al. Functional genomic characterization of delipidation elicited by *trans*-10, *cis*-12-conjugated linoleic acid (t10c12-CLA) in a polygenic obese line of mice. *Physiol. Genomics* **21**, 351–361 (2005).
33. Van, R. L., Bayliss, C. E. & Roncari, D. A. Cytological and enzymological characterization of adult human adipocyte precursors in culture. *J. Clin. Invest.* **58**, 699–704 (1976).
34. Negrel, R., Grimaldi, P. & Ailhaud, G. Establishment of preadipocyte clonal line from epididymal fat pad of *ob*/*ob* mouse that responds to insulin and to lipolytic hormones. *Proc. Natl Acad. Sci. USA* **75**, 6054–6058 (1978).
35. Verges, B., Walter, T. & Cariou, B. Endocrine side effects of anti-cancer drugs: effects of anti-cancer targeted therapies on lipid and glucose metabolism. *Eur. J. Endocrinol.* **170**, R43–R55 (2014).
36. Zhang, Y. & Chua, S. Jr. Leptin function and regulation. *Compr. Physiol.* **8**, 351–369 (2017).
37. Leong, K. W., & Qiang, L. Targeting obesity: eliminating visceral fat. *Columbia Engineering Magazine* (spring 2022).

Methods

Animal studies

All the mice were on a C57BL/6J background maintained in the Columbia University animal facility at 23 ± 1 °C and 12 h light and dark cycle with *ad libitum* access to chow food (PicoLab Rodent 5053) and water. HFD containing 60% fat was purchased from Research Diets (D12492i). For the obesity prevention studies, male or female mice were fed HFD and i.p. injected with P-G3 (10 mg per kg of body weight) in phosphate-buffered saline (PBS) twice weekly for the indicated times. In the treatment of lean mice, six-week-old male mice were fed chow diet and i.p. injected with P-G3 twice weekly for six weeks. For the obesity treatment study, male mice were induced obesity after ten weeks of HFD feeding and then i.p. injected with NPs (10 mg per kg of body weight) three times weekly for another six weeks. Body weight was monitored weekly, and body composition was determined by EchoMRI. After 16 h fasting followed by 4 h re-feeding, the mice were killed by CO_2 euthanasia for tissue and plasma collection. Plasma insulin (Insulin ELISA, Mercodia), TGs (Thermo Scientific) and NEFA (Fujifilm Wako) were accordingly measured. To measure lipid absorption, the lipid was extracted from faecal samples, as described previously[38], and the free fatty acid content (NEFA, Fujifilm Wako) was determined. The Columbia University Animal Care and Utilization Committee approved all the animal studies.

Metabolic phenotyping

For the indirect calorimetric study, a separate cohort of male mice were subjected to the Comprehensive Lab Animal Monitoring System (Columbus Instruments) after three P-G3 injections since the beginning of HFD feeding. For the glucose tolerance test (GTT), mice were fasted in a clean bedding cage for 16 h and then i.p. injected with glucose (2 g per kg of body weight). Blood glucose was measured using a Breeze 2 glucometer (Bayer) at the indicated time points. For the insulin tolerance test (ITT), mice were fasted for 4 h and i.p. injected with insulin (0.75 U per kg of body weight). For the lipid tolerance test, mice were fasted for 4 h and then given olive oil (200 µl per mice) by an oral gavage. The blood samples were taken by tail vein bleeding at the indicated time points. Thereafter, the serum lipid contents were accordingly measured. For lipolysis, the mice were i.p. injected with isoproterenol (10 mg per kg of body weight) and blood was collected through tail vein bleeding, and serum NEFA (Fujifilm Wako) and glycerol (Sigma, F6428) levels were accordingly measured.

Adipose-tissue ECM isolation

WAT was decellularized following a previously described method with modifications[39]. Briefly, tissue was placed in a 50 ml centrifuge tube containing 0.02% trypsin–0.05% ethylenediaminetetraacetic acid solution with orbital shaking at 37 °C for 30 min, then incubated with a new trypsin–ethylenediaminetetraacetic acid solution for another 30 min digestion. Next, the tissue was sequentially incubated in the following solutions at room temperature (RT) with shaking: 3% Triton X-100 for 1 h, 4% deoxycholic acid solution for 1 h, and 4% ethanol and 0.1% peracetic acid for 2 h. The tissue was rinsed in distilled deionized water (ddH_2O) between solution changes. The tissue was then washed at RT in PBS (pH 7.4) for 15 min three times, then in ddH_2O for 15 min three times and in 100% *n*-propanol for 30 min twice. Last, the tissue was washed four times with ddH_2O for 1 h before being ready to use.

Cy5-labelled P-G3 imaging

Ex vivo tissue distribution imaging: the mice were fed with HFD for five days to eliminate the possible trace background signal from the chow diet and then the tissues were collected. The tissues and ECM from iWAT and eWAT were incubated in PBS with or without Cy5-labelled P-G3 (100 µg in 30 ml) for 45 min with shaking at 37 °C. Afterwards, the tissues were washed with PBS for four times and then subjected to imaging analysis using PerkinElmer IVIS Spectrum optical imaging system (Living Image 4.5.5 software).

In vivo tissue distribution imaging: chow-fed or HFD-fed mice were injected with Cy5-labelled polymers or NPs (200 µg per mice) via i.p. or intravenous routes, or locally into iWAT. At the given time points, the mice were subjected to in vivo imaging by using the PerkinElmer IVIS system (Living Image 4.5.5 Software). The mice were then killed, and tissue signals were measured by using the same system.

Cell culture and adipocyte differentiation

3T3-L1 (ATCC CL-173) and C3H10T1/2 (CCL-226) cells were purchased from ATCC and cultured in high-glucose Dulbecco's modified Eagle medium supplemented with 10% calf serum (Gemini Bio-Products 100–506) or foetal bovine serum (heat inactivated; Corning 35-011-CV) and 1× penicillin–streptomycin (Thermo Fisher). The cells were differentiated in the standard adipogenic cocktail after reaching confluence for two days. The cocktail contains Dulbecco's modified Eagle medium, 10% foetal bovine serum, 1 µM dexamethasone, 10 µg ml^{-1} insulin and 0.5 mM 3-isobutyl-1-methylxanthine. Furthermore, 5 µM rosiglitazone was used in the first two days to facilitate C3H10T1/2 cells' differentiation. After induction for two days, the cells were maintained in a complete medium containing 2.5 µg ml^{-1} insulin until fully differentiated. P-G3 polymers or NPs (10 µg ml^{-1}) were added at the indicated times, and the cells were harvested during differentiation for analyses. The lipid droplets were visualized using Oil Red O staining or BODIPY staining. 3T3-L1 cells were treated with rapamycin (100 nM) from day 4 to day 6. C3H10T1/2 cells were treated with rapamycin (100 nM) from day 4 to day 9 for long-term rapamycin function analyses. 3T3-L1 cells were treated with NMN (20 mM) during day 0 to day 3 of differentiation and harvested on day 4 for analyses.

Human preadipocytes were cultured and differentiated following a previously published protocol[40]. The cells were differentiated in a complete differentiation medium with or without P-G3 (10 µg ml^{-1}) from day 0 to day 7, and then switched to a maintenance medium with or without P-G3 from day 7. The cells were harvested at day 7 or day 9 of differentiation for further gene expression analysis.

Human fat explant treatment

The protocol for collecting human fat biopsy has been reviewed and approved by the Weill Cornell Medicine Institutional Review Board (19-05020126). Fresh human omental adipose tissue was minced into small pieces (about 10 mg), washed with RT PBS and cultured in Medium 199 supplemented with 50 µg ml^{-1} gentamicin, 7 nM insulin and 25 nM dexamethasone[41], at the same time treated with or without 10 µg ml^{-1} P-G3. The medium was replaced every three days and the tissues were harvested on day 8 of treatment for RNA analysis.

Oil Red O staining

Differentiated adipocytes were rinsed with PBS twice and then fixed in 4% formalin-buffered solution for 30 min. Next, the fixed cells were washed with water twice, followed by covering with 60% isopropanol for 5 min and then stained with freshly made and filtered 60% Oil red O isopropanol solution for 15 min. The cells were then washed with distilled water and imaged.

Early endosome staining

C3H10T1/2 cells were plated on a cover glass in a six-well plate (Corning, 22 mm × 22 mm, No. 1) and differentiated using the protocol described above. An early endosome marker (CellLight Early Endosomes-GFP, BacMam 2.0, Thermo Fisher Scientific; 12 µl in each well) was added into the cell medium to stain the early endosomes overnight. After washing with PBS, Cy5-labelled P-G3 or Cy5-labelled NPs were added to the culture medium with a final concentration of 100 µg ml^{-1}. After 15 min or 1 h incubation, Cy5-labelled P-G3 or Cy5-labelled NPs were removed, and then the cells were rinsed with PBS and fixed in 4% paraformaldehyde. The nuclei were stained with DAPI (4′,6-diamidino-2-phenylindole). The images were taken on a Nikon A1 confocal microscope.

Cellular organelle staining

Mature 3T3-L1 cells were plated into a four-well Lab-Tek II chambered cover glass (Thermo Fisher Scientific). Cy5-labelled P-G3 was added to the culture medium with a final concentration of 10 μg ml^{-1}. After 24 h, the cells were changed with a fresh medium containing 50 nM LysoTracker Red DND-99 (Thermo Fisher Scientific) or 100 nM MitoTracker Red CMXRos (Cell Signalling Technology) to stain the lysosome or mitochondria, respectively, for 30 min. For endoplasmic reticulum staining, the cells were rinsed with Hank's balanced salt solution with calcium and magnesium, and 1 μM ER-Tracker Red dye (Thermo Fisher Scientific) was added together with Hoechst 33243 for nucleus staining in live cells. For the staining of lipid droplets, the cells were fixed with 4% paraformaldehyde, washed with PBS and then incubated in 1 μM BODIPY 493/503 (Thermo Fisher Scientific) for 5 min followed by washing with PBS for three times. The images were taken on a ZEISS Axio Observer 7 instrument.

P-G3 coating on carboxylate microbeads

Excess P-G3 polymers were added to the carboxylate microbeads (Polybead Carboxylate Microspheres 6.00 μm, Polysciences) in a microcentrifuge tube, briefly vortexed and incubated with shaking overnight at 4 °C. The microbeads were washed with cell-culture-grade water and then spun down at 4 °C at 10,000×*g* for 5 min. After washing three times, the precipitated microbeads were resuspended in cell-culture-grade water of the original volume, and the surface potential was measured with Malvern Zetasizer Nano ZS90. To quantify the P-G3 contents on the microbeads, Cy5-labelled P-G3 was used following the procedure above. The P-G3 amount was determined according to the standard curve. 3T3-L1 cells were differentiated in 12-well transwell plate (Corning). Then, 10 μg ml^{-1} P-G3 or microbeads containing an equal amount of P-G3 were directly added in the medium. In the transwell group, the microbeads were separated from cells by an insert of 0.4 μm pore size.

NP synthesis and characterization

Here 15 μmol P-G3 (Sigma-Aldrich) in 5 ml methanol (Thermo Fisher Scientific) was mixed with 75 μmol cholesterol chloroformate (Sigma-Aldrich) in 5 ml dichloromethane (Thermo Fisher Scientific), followed by the addition of 300 μmol *N*,*N*-diisopropylethylamine (Sigma-Aldrich). The mixture was then stirred at 50 °C for 3 h, and dialysed in ultrapure water for 72 h to generate P-G3-Chol(5). To fabricate P-G3-Chol(5) NPs, 1 mg P-G3-Chol(5) was dissolved in 200 μl chloroform (Thermo Fisher Scientific), followed by the addition of 1 ml H_2O and sonication for 2 min. Finally, 5 ml H_2O was added into the mixture, and the excess solvent was removed by using a rotary evaporator to generate P-G3-Chol(5) NPs. The structure of the resulting NPs was characterized by a Bruker Avance III 400 NMR instrument. The morphology was imaged using a Titan Themis 200 transmission electron microscope. The hydrodynamic diameter and zeta potential of the NPs were measured by a Malvern Nano ZS90 Zetasizer. The absorbance was measured using a Denovix DS-11+ spectrophotometer.

NAD^+ cellular concentration

Preadipocytes or adipocytes were treated with P-G3 (10 μg ml^{-1}) or PBS for 14 h, and the cellular NAD^+/NADH levels were determined by the NAD^+/NADH quantitation colorimetric kits (BioVision K337) following the manufacturer's instructions.

Gene expression analysis

Total RNA from the tissues or cells was extracted using the TRIzol reagent (Thermo Fisher) in combination with an RNA isolation kit from MACHEREY-NAGEL. Here 1 μg RNA was used for reverse transcription to synthesize cDNA by using a high-capacity cDNA reverse transcription kit (Applied Biosystems). Bio-Rad CFX96 real-time polymerase chain reaction (PCR) system was used to perform quantitative real-time polymerase chain reaction (qPCR) with GoTaq qPCR Master Mix (Promega). The relative gene expression was calculated by using the ΔΔCt method with *Cyclophilin A* or *Rpl23* as the reference gene. The primer sequences are available in Supplementary Tables 4 and 5.

scRNA-seq

3T3-L1 cells were cultured and differentiated as described above. P-G3 (10 μg ml^{-1}) or PBS was added to the cells since day 0 of differentiation. Cells were collected at differentiation day 0, 3 and 6 as preadipocytes, early adipogenesis and mature adipocytes, respectively (Supplementary Table 1). At collection, the cells were gently dissociated into single cells with trypsin enzymatic digestion. The cell viability was confirmed over 85% by trypan blue exclusion before subjecting for scRNA-seq using 10x Genomics Chromium technology. The resulting single-cell 3′-end cDNA libraries were sequenced on Illumina NovaSeq 6000 sequencing system (2 × 100 bp pair-end) at the Single Cell Analysis Core of the Columbia Genome Center. Here 10x Genomics' Cell Ranger pipeline (v. 3.1.0) with mouse reference transcriptome GRCm38 was used to process the data. Details of sample information for scRNA-seq are listed in Supplementary Table 2. In samples containing mature adipocytes (LQ004 and LQ005), the cell suspension media also contained lipid droplets. The lipid droplets were coincidently barcoded, too. This was the reason for the high expected number from the sequencer with low mean reads in LQ004 and LQ005. We excluded the lipid droplet noise in sequencing data by only keeping the cells with gene numbers (2,500 to 9,000 genes) and mitochondria gene percentage less than 20% for downstream analysis. Details of the software and algorithms can be found in Supplementary Table 3.

RNA velocity and regulatory network analysis

Preprocessing of the single-cell analysis for normalization and unsupervised clustering was performed with Scanpy (v. 1.7.1) in Python (v. 3.6). We annotated the cell types based on known adipogenesis and lipogenesis markers. We classified the subgroup of the mature adipocytes as lipogenic adipocytes when a high expression of lipid accumulation genes was observed. Overall, four cell types were observed in our dataset: preadipocytes, immature adipocytes, adipocytes and lipogenic adipocytes (Fig. 4b, Extended Data Fig. 5a and Supplementary Table 1). Next, we computed the RNA velocities (rate of splicing and degradation) based on spliced and unspliced mRNA dynamics of every single cell using scVelo (v. 0.2.1) and velocyto (v. 0.17.16) (Fig. 4e–h and Extended Data Fig. 5d,e). Regulatory networks were identified by the coexpression pattern of transcription factor and its downstream effector genes by SCENIC (v. 1.2.2) (Extended Data Fig. 5c). The methods for recovering the RNA velocity and regulons are insensitive to data normalization. We used raw sequencing data and cell-type annotations as inputs to perform the above analysis.

Altered gene pathway analysis

We used QIAGEN IPA software to calculate the statistical significance (Fig. 4i). In brief, the IPA software used Fisher's exact test to calculate the overlap of our dataset with the reference database (that is, sets of molecules in canonical pathways). The *p* value measures the likelihood of an observed association between our experimental dataset and a specific canonical pathway due to random chance. The corresponding pathway is significantly associated with the experiment dataset when the *p* value is small (that is, $p < 0.05$).

Lysosomal intracellular activity analysis

The lysosomal activity was determined by using the BioVision lysosomal intracellular activity assay kit (k448-50). In brief, C3H10T1/2 cells were pretreated with or without P-G3 from differentiation day 5 to day 7. Bafilomycin A1 was used as a lysosome inhibitor control. The cells were then incubated in a cell medium supplemented with 0.5% foetal bovine serum and self-quenched substrate for 2 h, followed by the addition of an assay buffer to terminate the experiment. The cells were then

dissociated and subjected to flow cytometry analysis (488 nm excitation laser). The gating strategy is shown in Extended data Fig. 6e. Flow cytometry data were analysed by FCS Express (v. 7.14.0020) software.

Western blotting

Cells or tissues were lysed with a total protein lysis buffer supplemented with protease and phosphatase inhibitor cocktail. The protein supernatants were subjected to protein quantification using a Pierce BCA kit and 10% gel sodium dodecyl sulfate–polyacrylamide gel electrophoresis separation. Antibodies used in this study are as follows: p-mTOR (CST #2971), p-S6K (CST #9205), p-4E-BP1 (CST #2855), p-AKT (Ser 473, CST #9271), p-AKT (T308, CST #13038), p-GSK3b (Ser 9, CST #9322), FASN (CST #3180), ADIPSIN (R&D Systems, #AF5430), Adiponectin (Thermo Fisher, #PA1-054), CEBPA (Santa Cruz, sc-61), HSP90 (Proteintech, #13171-1-AP) and GAPDH (Proteintech #HRP-60004). The dilution of antibodies was based on the recommendation on the manufacturer's website.

Histological assessments

After dissection, eWAT, iWAT and liver were immediately fixed in 10% formalin-buffered solution. After fixation and dehydration, tissues were embedded into paraffin, stained with antibody against F4/80 (CST, #70076), haematoxylin and eosin (H&E) or periodic acid–Schiff, and photographed under a microscope (Olympus IX71). For immunohistochemistry, eWAT, iWAT and liver were immediately fixed in 4% paraformaldehyde at 4 °C overnight, and then dehydrated in 30% sucrose at RT overnight followed by embedding into an optimum cutting temperature medium (Sakura Tissue-Tek O.C.T. compound 4583). After mounting in 5 µm slides, the frozen sections were incubated with antibody caveolin-1 (D46G3) (CST, #3267; 1:250 dilution) and then anti-rabbit Alexa 488 antibody (Thermo Fisher Scientific, #A27034; 1:1,000 dilution), and further imaged by confocal microscopy. The images were processed using the ImageJ software (v. 2.1.0; National Institutes of Health).

Statistical analysis

The significance between the groups was evaluated using a two-tailed Student's *t*-test. The difference between the groups is statistically significant if the *p* value is less than 0.05. In this study, all the data are represented as mean ± standard error of the mean (s.e.m.). Prism 9.3.1 (GraphPad) was used for the analysis.

Reporting summary

Further information on research design is available in the Nature Portfolio Reporting Summary linked to this article.

Data availability

The single-cell RNA-seq data are available in the Gene Expression Omnibus (GEO) database under accession number GSE209819. Sample information and sequencing statistics are described in Supplementary Tables 1 and 2. All the remaining data are available from the corresponding authors upon reasonable request. Source data are provided with this paper.

References

38. Higuchi, S. et al. Bile acid composition regulates GPR119-dependent intestinal lipid sensing and food intake regulation in mice. *Gut* **69**, 1620–1628 (2020).
39. Brown, B. N. et al. Comparison of three methods for the derivation of a biologic scaffold composed of adipose tissue extracellular matrix. *Tissue Eng. Part C Methods* **17**, 411–421 (2011).
40. Lee, M. J. & Fried, S. K. Optimal protocol for the differentiation and metabolic analysis of human adipose stromal cells. *Methods Enzymol.* **538**, 49–65 (2014).
41. Lee, M. J., Gong, D. W., Burkey, B. F. & Fried, S. K. Pathways regulated by glucocorticoids in omental and subcutaneous human adipose tissues: a microarray study. *Am. J. Physiol. Endocrinol. Metab.* **300**, E571–E580 (2011).

Acknowledgements

We thank S. K. Fried for kindly providing the human primary adipocytes, L. Yang for scientific discussion and help with designing the schematic and C. H. Quek for all the technical support and scientific suggestions. The studies used the resources of the Diabetes and Endocrinology Research Center Flow Core Facility funded in part through Center Grant 5P30DK063608 and the Maurice Hurd and the Weill Cornell Biorepository Core. The in vivo and in vitro imaging and processing used resources at the Oncology Precision Therapeutics and Imaging Core (OPTIC) (HICCC). This work was supported by the Russell Berrie Foundation (L.Q. and Q.W.), Blavatnik SIRS funding (L.Q. and K.W.L.), National Institutes of Health grant RO1AR073935 and USAMR grant W81XWH1910463 (K.W.L.), and The Manoogian Simone Foundation (M.D.G.).

Author contributions

Q.W., B.H. and L.Q. designed and performed the research. Y.X. performed the scRNA analyses. T.L. prepared the cationic materials. Y.H. performed the NAD quantification in cells. W.D. performed the confocal imaging. Q.W., B.H., T.L., Y.X., Y.H., W.D. and B.Z.W. provided the experimental data. M.D.G., G.F.D. and S.C. contributed to the human fat biopsy studies and M.R. participated in the discussion and manuscript editing. Q.W., B.H., Y.X., K.W.L. and L.Q. wrote and revised the paper.

Competing interests

A patent application (inventors: L.Q., K.W.L., Q.W., B.H., T.L.) was filed in the U.S.A. (Application number: 63309325). The remaining authors declare no competing interests.

Additional information

Extended data is available for this paper at https://doi.org/10.1038/s41565-022-01249-3.

Supplementary information The online version contains supplementary material available at https://doi.org/10.1038/s41565-022-01249-3.

Correspondence and requests for materials should be addressed to Kam W. Leong or Li Qiang.

Peer review information *Nature Nanotechnology* thanks Omid Farokhzad and the other, anonymous, reviewer(s) for their contribution to the peer review of this work.

https://doi.org/10.1038/s41565-022-01249-3

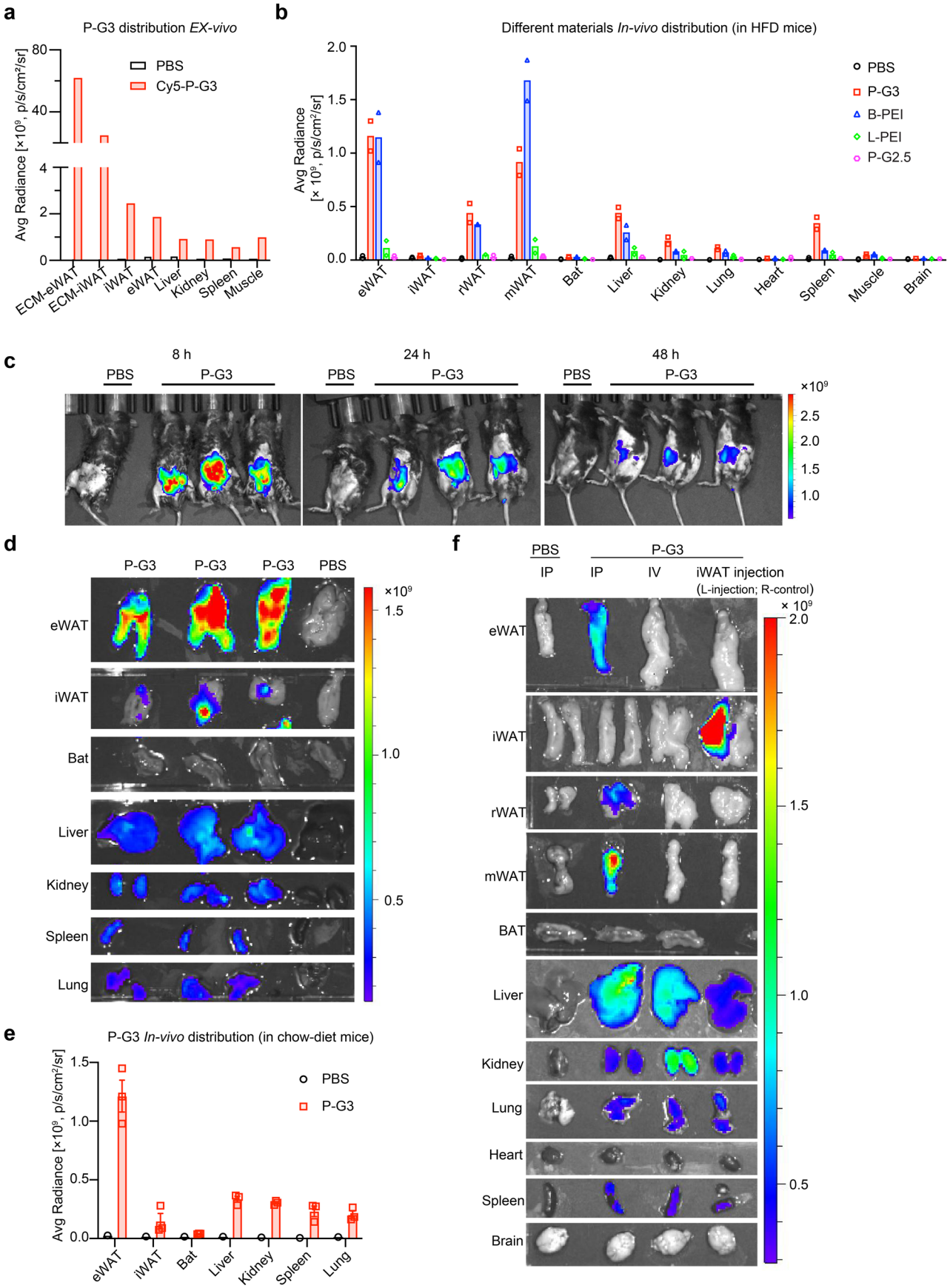

Extended data Fig. 1 | See next page for caption.

https://doi.org/10.1038/s41565-022-01249-3

Extended data Fig. 1 | Selective biodistribution of P-G3 to visceral fat. a, Cy5 signal quantification of different tissues in Fig. 1a. **b**, Tissue distribution quantification of different materials in Fig. 1h–i: vehicle (n = 2), all the treatment groups (n = 2). **c**–**e**, 200 μg Cy5-labled P-G3 was i.p. injected into chow-fed mice and fluorescent signals were determined using an IVIS Optical Imager. PBS was used as vehicle control. **c**, Signal in live animals during the treatment at indicated time; imaging of tissues from mice sacrificed at 56-hr post-injection (**d**) and quantification of fluorescent signals, vehicle (n = 1), P-G3 group (n = 3). Data were represented as mean ± s.e.m. (**e**). **f**, 200 μg Cy5-labled P-G3 was injected into HFD-fed mice comparing different delivery routes, and Cy5 signal in tissues was determined at 24-hr post-injection. The unit of fluorescent scale bar is photons/sec/cm^2/sr.

https://doi.org/10.1038/s41565-022-01249-3

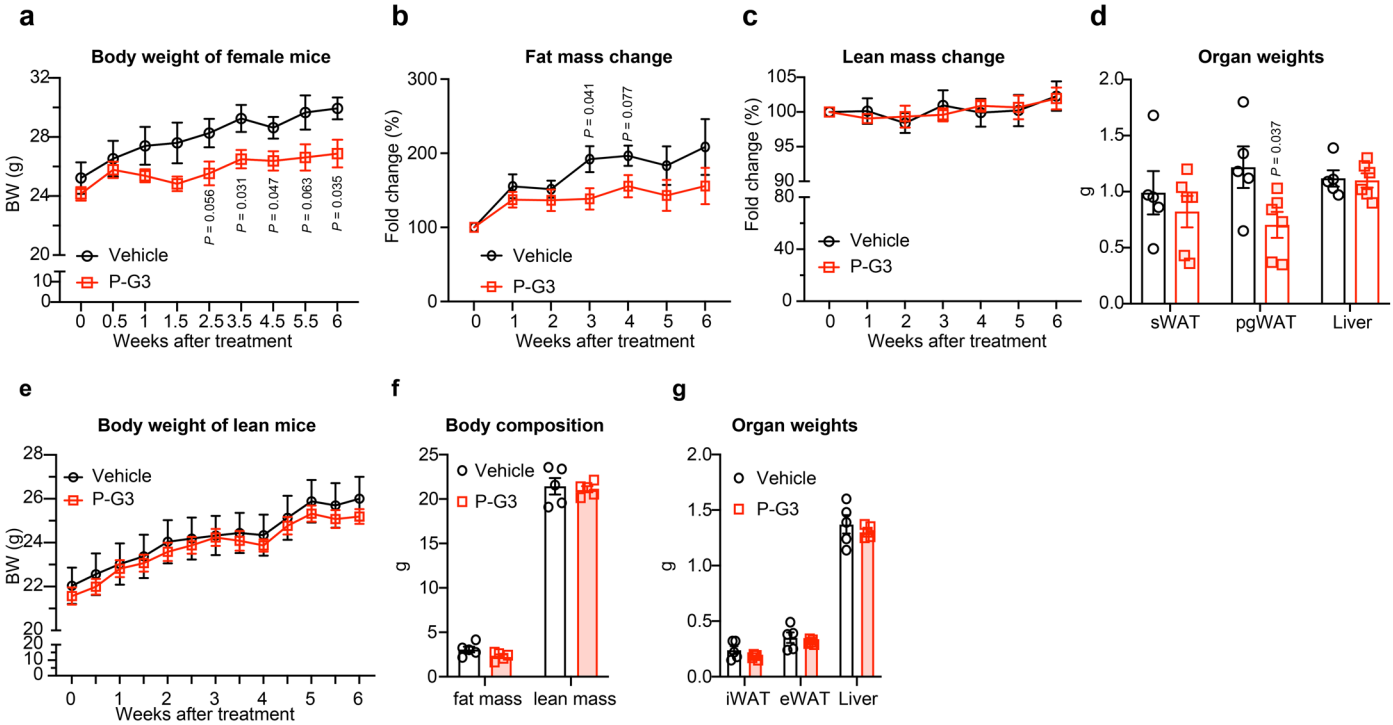

Extended data Fig. 2 | The anti-obesity effect of P-G3 is reproduced in diet-induced obese female mice but not in lean animals. a–**d**, 17-wk-old female C57BL/6J mice were intraperitoneally treated with P-G3 (10 mg/kg.BW) or vehicle twice weekly for 6 weeks since the beginning of HFD feeding. Data were represented as mean ± s.e.m. ($n = 5, 6$). Statistical significance was calculated via 2-tailed Student's *t*-test. **a**, Body weight curve. **b**, **c**, Changes of fat mass (**b**) and lean mass (**c**) during P-G3 treatment determined by Echo-MRI. **d**, Organ weights at sacrifice. **e**–**g**, 6-wk-old male mice were fed on chow diet and received twice weekly P-G3 (10 mg/kg.BW) intraperitoneally for 6 weeks. Data were represented as mean ± s.e.m. ($n = 5, 5$). Statistical significance was calculated via 2-tailed Student's *t*-test. **e**, Body weight curve. **f**, Body composition determined by EchoMRI. **g**, Organ weights at sacrifice.

https://doi.org/10.1038/s41565-022-01249-3

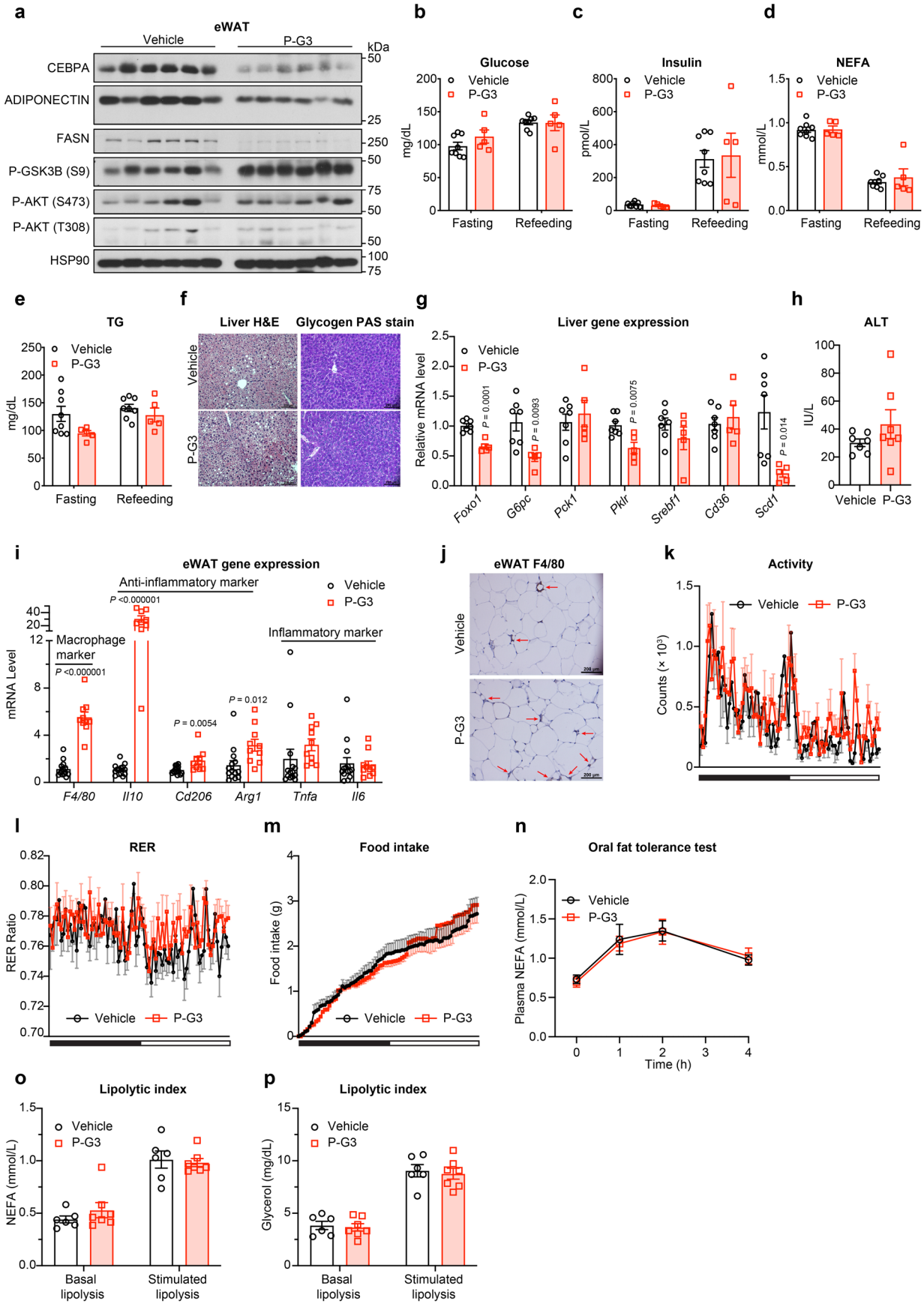

Extended data Fig. 3 | See next page for caption.

https://doi.org/10.1038/s41565-022-01249-3

Extended data Fig. 3 | P-G3 treatment improves metabolic health in DIO mice. **a**, Western blotting of adipocyte markers and insulin signalling proteins in the eWAT of DIO mice after P-G3 treatment. Representative data were repeated twice independently with similar results. **b**-**e**, Mice were treated with P-G3 since the beginning of HFD feeding in Fig. 2. Before sacrifice, mice were fasted overnight and then refed for 4 hours to measure plasma metabolites. Data were represented as mean ± s.e.m. (n = 8, 5). **f**, **g**, H&E and PAS staining of glycogen contents (**f**) and qPCR analysis of gene expression (**g**) in the liver. Data were represented as mean ± s.e.m. (n = 7, 5). Statistical significance was calculated via 2-tailed Student's t-test. **h**, Plasma alanine aminotransferase (ALT) level in another cohort of mice after P-G3 treatment for 6 weeks. Data were represented as mean ± s.e.m. (n = 7, 7). **i**, **j** Gene expression of inflammatory and anti-inflammatory markers (**i**) and F4/80 staining (**j**) in eWAT from mice with or without P-G3 treatment. Data were represented as mean ± s.e.m. (n = 14, 10). Statistical significance was calculated via 2-tailed Student's t-test. **k**-**m**, Male mice were received 3 dosages of P-G3 (10 mg/kg.BW) or vehicle (intraperitoneally) twice-weekly since the beginning of HFD feeding, then housed singly in metabolic cages for calorimetric analysis. **k**, Locomotor activity. **l**, Respiration exchange ratio (RER). **m**, Food intake within 1 dark/light cycle. Data were represented as mean ± s.e.m. (n = 7, 7). **n**, Oral fat tolerance test from mice after 6-wk P-G3 treatment. Data were represented as mean ± s.e.m. (n = 7, 7). **o**, **p**, Plasma NEFA (**o**) and glycerol (**p**) level in mice before and 15 min after the intraperitoneal injection of isoproterenol (10 mg/kg.BW). Data were represented as mean ± s.e.m. (n = 6, 7).

https://doi.org/10.1038/s41565-022-01249-3

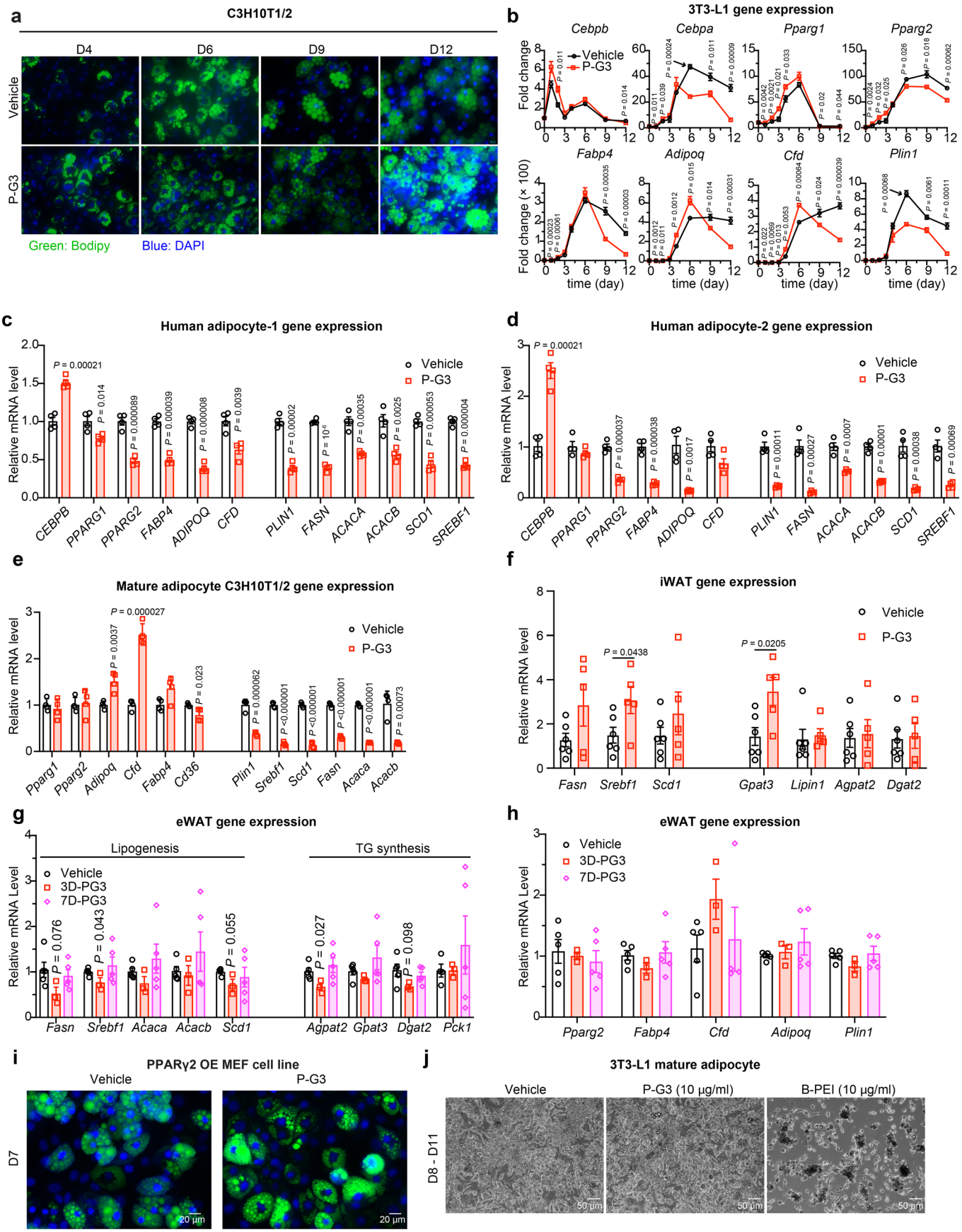

Extended data Fig. 4 | See next page for caption.

https://doi.org/10.1038/s41565-022-01249-3

Extended data Fig. 4 | P-G3 inhibits adipocyte hypertrophic growth. a, BODIPY staining of lipid accumulation in C3H10T1/2 cells during differentiation time course with or without P-G3 treatment. Representative data were repeated three times independently with similar results. **b**, qPCR analysis of gene expression of adipogenic markers during the time course of 3T3-L1 differentiation with or without P-G3 treatment. Data were represented as mean ± s.e.m. (n = 4, 4). Statistical significance was calculated via 2-tailed Student's t-test. **c**, **d**, Human adipose stromal cells were differentiated into adipocytes with or without P-G3 treatment, and qPCR analyses of gene expression in cells at Day 7 (**c**) or Day 9 (**d**) of differentiation. Data were represented as mean ± s.e.m. (n = 4, 4). Statistical significance was calculated via 2-tailed Student's t-test. **e**, C3H10T1/2 cells were fully differentiated into mature adipocytes and then treated with 10 μg/ml P-G3 from Day 15 to Day 21. qPCR analysis of gene expression. Data were represented as mean ± s.e.m. (n = 4, 4). Statistical significance was calculated via 2-tailed Student's t-test. **f**, qPCR analysis of gene expression in iWAT from mice after 8-wk P-G3 treatment. Data were represented as mean ± s.e.m. (n = 6, 5). Statistical significance was calculated via 2-tailed Student's t-test. **g**, **h**, Mice were fed on HFD diet for 4 weeks, then received vehicle or a single-dose P-G3 (intraperitoneally) and scarified at Day 3 or Day 7 post-injection. qPCR analysis of gene expression of lipogenic (**g**) and adipogenic (**h**) markers in the eWAT. Data were represented as mean ± s.e.m. (n = 5, 3, 5). Statistical significance was calculated via 2-tailed Student's t-test (treatment group vs vehicle group). **i**, PPARγ2-reconstituted Pparg-KO embryonic fibroblasts (MEFs) cells were differentiated into adipocytes in the presence or absence of P-G3. On Day 7 of differentiation, lipid droplet morphology was assessed by BODIPY staining. **j**, Mature adipocytes were treated with or without 10 μg/ml P-G3 or B-PEI from differentiation Day 8 to Day 11. Representative data in **i** and **j** were repeated twice independently with similar results.

https://doi.org/10.1038/s41565-022-01249-3

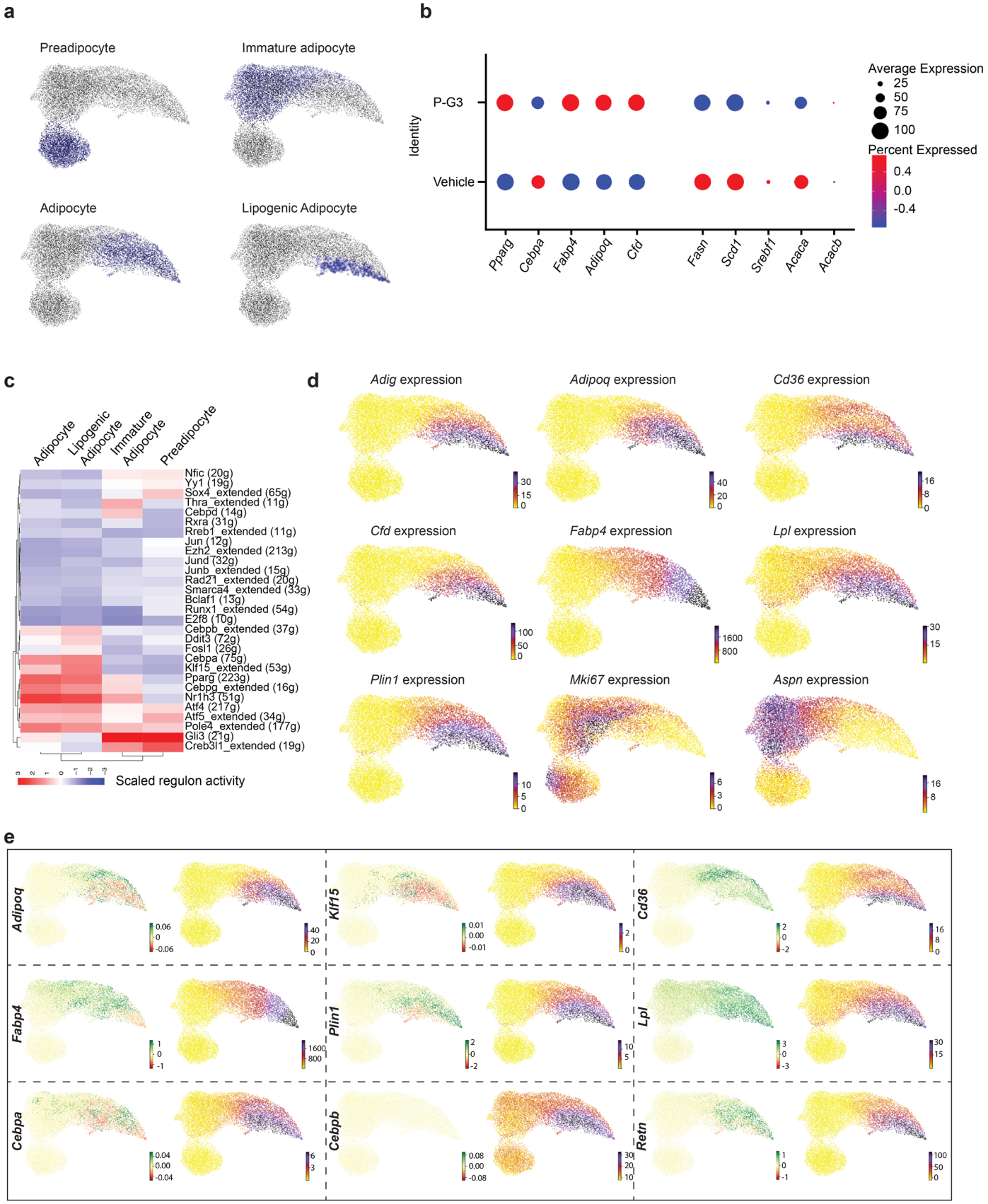

Extended data Fig. 5 | scRNA-seq analyses of adipocyte development. a, Heterogeneous cell distributions during 3T3-L1 adipogenesis. **b**, Dot-plot showing bifurcate regulation of key genes in adipogenesis (*Pparg*, *Cebpa*, *Fabp4*, *Adipoq*, and *Cfd*) and lipogenesis (*Fasn*, *Scd1*, *Srebf1*, *Acaca*, and *Acacb*) in P-G3-treated cells on Day 6 of differentiation. **c**, Key gene regulatory networks identified in each cell type. **d**, Expression of key cell type markers. **e**, Expression of spliced mature mRNA of representative adipocyte genes and their RNA velocity based on unspliced/spliced mRNA ratio.

https://doi.org/10.1038/s41565-022-01249-3

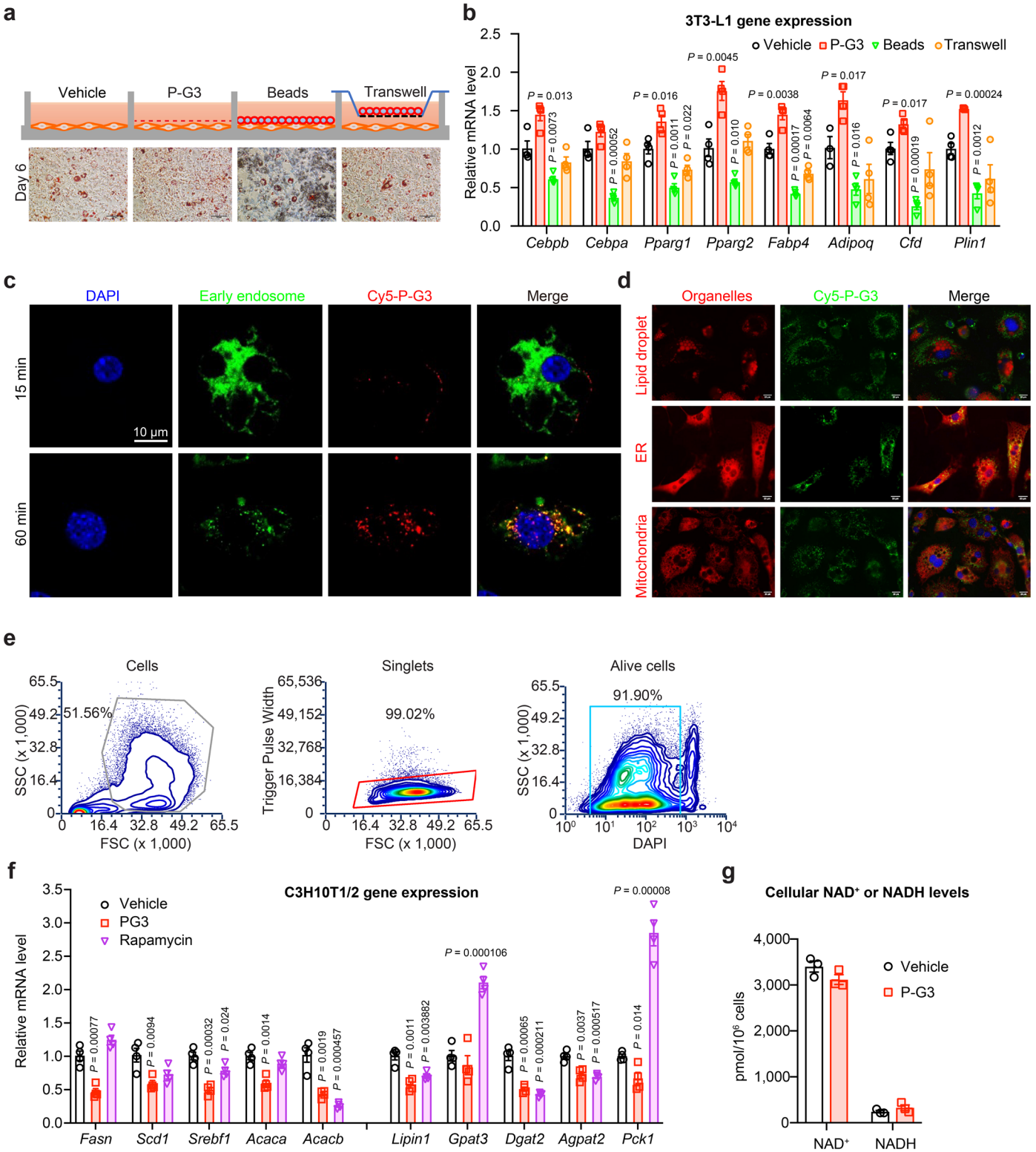

Extended data Fig. 6 | P-G3 enters cells to modulate mTOR and NAD signal pathways in adipocyte development. a, Schematic experiment design (top) and Oil Red O staining (bottom) of 3T3-L1 cells after the treatments of different localizations of P-G3. 3T3-L1 preadipocytes were differentiated in the presence of naked P-G3, microbead-conjugated P-G3 to prevent entering cells, or P-G3 beads in transwells to prevent the contact with cells. **b**, qPCR analyses of gene expression of cells in (a). Data were represented as mean ± s.e.m. ($n = 4, 4, 4, 4$). Statistical significance was calculated via 2-tailed Student's *t*-test (treatment group vs vehicle group). **c**, The internalization of Cy5-labelled P-G3 into early endosome. Confocal images of Cy5-labelled P-G3 with early endosome marker in mature C3H10T1/2 adipocytes after 15 min or 1 hr of Cy5-P-G3 treatment. **d**, Colocalization of Cy5-P-G3 with lipid droplet, ER, and mitochondria in mature 3T3-L1 adipocytes after 24-hr of Cy5-P-G3 treatment. Representative data in **c** and **d** repeated twice with similar results. **e**, Representative gating strategy used in FACS analysis of lysosomal activity in Fig. 5b. **f**, Gene expression in C3H10T1/2 cells after indicated treatments from differentiation Day 4 to Day 9. Data were represented as mean ± s.e.m. ($n = 4, 4$). Statistical significance was calculated via 2-tailed Student's *t*-test (treatment group vs vehicle group). **g**, P-G3 failed to affect NAD^+ and NADH levels in mature adipocytes after 14-hr treatment. Data were represented as mean ± s.e.m. ($n = 3, 3$).

https://doi.org/10.1038/s41565-022-01249-3

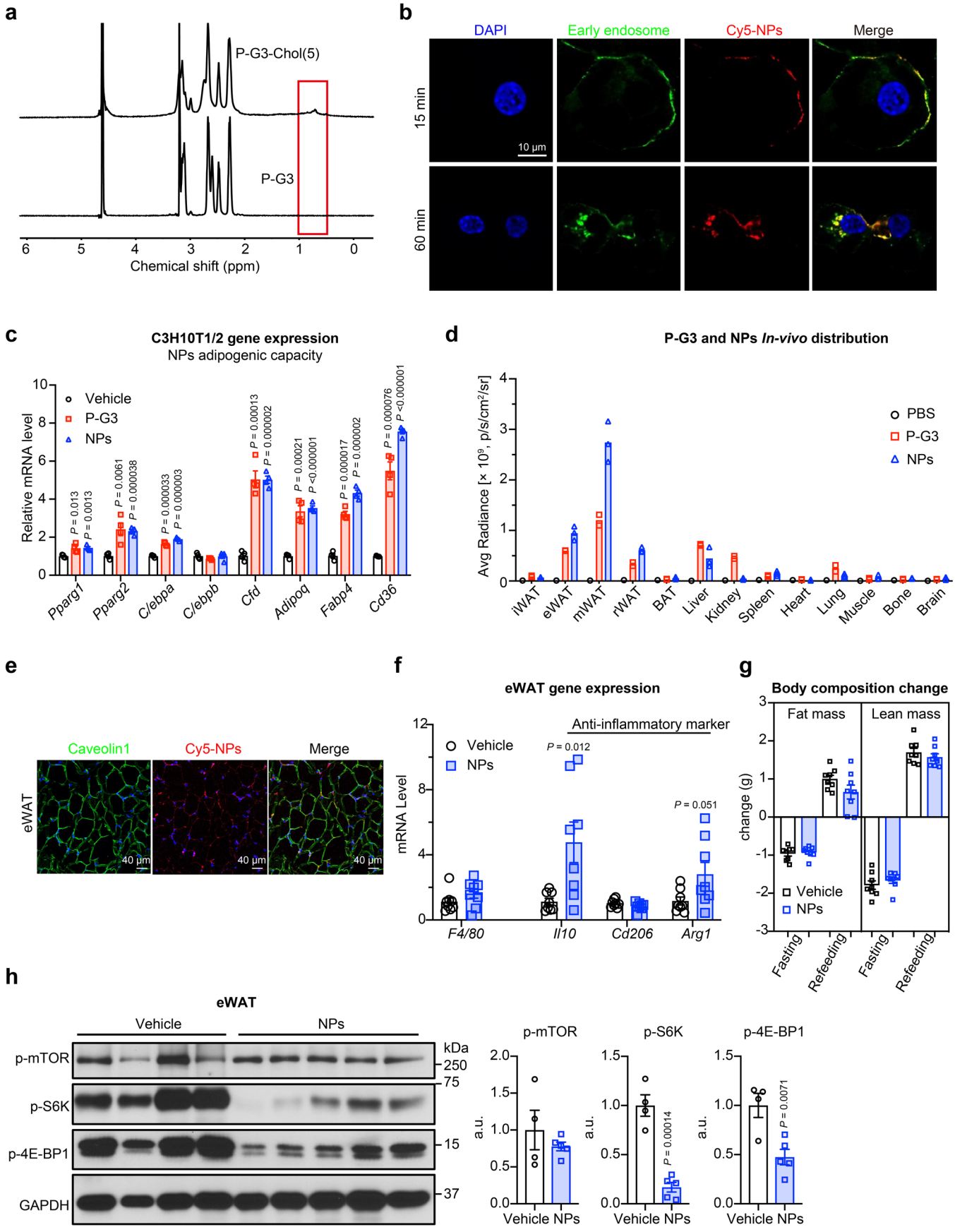

Extended data Fig. 7 | See next page for caption.

https://doi.org/10.1038/s41565-022-01249-3

Extended data Fig. 7 | Lipophilic P-G3 NPs retains the effects of P-G3. a, NMR spectrum of P-G3 and P-G3-Chol(5). **b**, The internalization of Cy5-labelled NPs into early endosome. Confocal images of Cy5-labelled NPs with early endosome marker in mature C3H10T1/2 adipocytes after 15 min or 1 hr of Cy5-NPs treatment. Representative data repeated twice with similar results. **c**, C3H10T1/2 preadipocytes were treated with 10 μg/ml P-G3 or NPs since the induction of differentiation Day 0, and cells were harvested on Day 4 to measure adipogenic genes by qPCR. Data were represented as mean ± s.e.m. (n = 4, 4). Statistical significance was calculated via 2-tailed Student's t-test (treatment group vs vehicle group). **d**, **e**, 200 μg Cy5-labled NPs or Cy5-labelled P-G3 were i.p. injected into mice in Fig. 6c; **d**, signal intensity quantification of tissue distribution and at 72-hr post-injection by IVIS (PBS group n = 1, P-G3 group n = 2, NPs group n = 3); **e**, colocalization of Cy5-labelled NPs with DAPI and Caveolin-1 in frozen sections of eWAT. **f**, Macrophage-related gene expression in the eWAT after NP treatment. Data were represented as mean ± s.e.m. (n = 8, 8). Statistical significance was calculated via 2-tailed Student's t-test. **g**, Body composition change of NPs-treated DIO mice during 24-hr fasting and 24-hr refeeding. Data were represented as mean ± s.e.m. (n = 8, 8). **h**, WB analysis of mTOR signalling pathway in eWAT after NPs treatment and the quantification. Data were represented as mean ± s.e.m. (n = 4, 5). Statistical significance was calculated via 2-tailed Student's t-test.

nature portfolio

Corresponding author(s): Li Qiang

Last updated by author(s): Sep 19, 2022

Reporting Summary

Nature Portfolio wishes to improve the reproducibility of the work that we publish. This form provides structure for consistency and transparency in reporting. For further information on Nature Portfolio policies, see our Editorial Policies and the Editorial Policy Checklist.

Statistics

For all statistical analyses, confirm that the following items are present in the figure legend, table legend, main text, or Methods section.

n/a	Confirmed
☐	☒ The exact sample size (*n*) for each experimental group/condition, given as a discrete number and unit of measurement
☐	☒ A statement on whether measurements were taken from distinct samples or whether the same sample was measured repeatedly
☐	☒ The statistical test(s) used AND whether they are one- or two-sided *Only common tests should be described solely by name; describe more complex techniques in the Methods section.*
☒	☐ A description of all covariates tested
☒	☐ A description of any assumptions or corrections, such as tests of normality and adjustment for multiple comparisons
☐	☒ A full description of the statistical parameters including central tendency (e.g. means) or other basic estimates (e.g. regression coefficient) AND variation (e.g. standard deviation) or associated estimates of uncertainty (e.g. confidence intervals)
☐	☒ For null hypothesis testing, the test statistic (e.g. *F*, *t*, *r*) with confidence intervals, effect sizes, degrees of freedom and *P* value noted *Give P values as exact values whenever suitable.*
☒	☐ For Bayesian analysis, information on the choice of priors and Markov chain Monte Carlo settings
☒	☐ For hierarchical and complex designs, identification of the appropriate level for tests and full reporting of outcomes
☒	☐ Estimates of effect sizes (e.g. Cohen's *d*, Pearson's *r*), indicating how they were calculated

Our web collection on statistics for biologists contains articles on many of the points above.

Software and code

Policy information about availability of computer code

Data collection	No software was used to collect data.
Data analysis	Softwares for Single cell seq analysis include Cell Ranger (v3.1.0), R (v3.6.3), Python (v3.6), Scanpy(v1.7.1), Seurat (v3.1.1), Velocyto(v0.17.16), scVelo (v0.2.1), SCENIC (v1.2.2) listed in supplementary table 3. Cy5-labeled P-G3 or NPs in living mice or tissues were imaged and analyzed using PerkinElmer IVIS Spectrum Optical Imaging System (Living Image 4.5.5 Software). Most data were analyzed with Prism 9.3.1 (GraphPad) software. Tissue slides and cell Images were processed using ImageJ 2.1.0 (National Institutes of Health) software. Flow cytometry data were analyzed by FCS Express (7.14.0020) software.

For manuscripts utilizing custom algorithms or software that are central to the research but not yet described in published literature, software must be made available to editors and reviewers. We strongly encourage code deposition in a community repository (e.g. GitHub). See the Nature Portfolio guidelines for submitting code & software for further information.

Data

Policy information about availability of data

All manuscripts must include a data availability statement. This statement should provide the following information, where applicable:

- Accession codes, unique identifiers, or web links for publicly available datasets
- A description of any restrictions on data availability
- For clinical datasets or third party data, please ensure that the statement adheres to our policy

The single-cell RNA-seq data are available in the Gene Expression Omnibus (GEO) database under accession number GSE209819.

Human research participants

Policy information about studies involving human research participants and Sex and Gender in Research.

Reporting on sex and gender	The biomaterial used in this study was from one female subject.
Population characteristics	Only sample from one subject was used.
Recruitment	The subject's biomaterial was obtained from a cross-sectional study (Next Generation Sequencing for Diabetes and Metabolic Diseases study). Participants of this study were recruited from one of six Weill Cornell Medicine clinics, including Bariatric Surgery, Endocrinology, Gastroenterology, Cardiology, and Internal Medicine from August 2020 – July 2022. Inclusion criteria included a diagnosis of hyperlipidemia, Type-2 Diabetes, Pre-diabetes, or Non-alcoholic Fatty Liver Disease/Non-alcoholic Steatohepatitis.
Ethics oversight	The study has been approved by Weill Cornell Medicine IRB 19-05020126.

Note that full information on the approval of the study protocol must also be provided in the manuscript.

Field-specific reporting

Please select the one below that is the best fit for your research. If you are not sure, read the appropriate sections before making your selection.

☒ Life sciences ☐ Behavioural & social sciences ☐ Ecological, evolutionary & environmental sciences

For a reference copy of the document with all sections, see nature.com/documents/nr-reporting-summary-flat.pdf

Life sciences study design

All studies must disclose on these points even when the disclosure is negative.

Sample size	Sample sizes for experiments were estimated based on previous experiences and reports with similar setups to achieve 80% power of significance.
Data exclusions	No data were excluded from the analyses.
Replication	All the in vitro were repeated at least three times with similar results. Key in vivo experiments were repeated at least two times with similar results.
Randomization	Animals were assigned randomly to experimental and control groups. Cells were also randomly assigned to experimental groups with different treatments.
Blinding	Histological assessments, flow cytometry analysis, and data collection of single cell sequence were performed in blinded manner.

Reporting for specific materials, systems and methods

We require information from authors about some types of materials, experimental systems and methods used in many studies. Here, indicate whether each material, system or method listed is relevant to your study. If you are not sure if a list item applies to your research, read the appropriate section before selecting a response.

Materials & experimental systems

n/a	Involved in the study
☐	☒ Antibodies
☐	☒ Eukaryotic cell lines
☒	☐ Palaeontology and archaeology
☐	☒ Animals and other organisms
☒	☐ Clinical data
☒	☐ Dual use research of concern

Methods

n/a	Involved in the study
☒	☐ ChIP-seq
☐	☒ Flow cytometry
☒	☐ MRI-based neuroimaging

Antibodies

Antibodies used

Antibodies used in this study are:
p-mTOR, Cell signaling technology, catalog number: CST #2971;
p-S6K, Cell signaling technology, catalog number: CST #9205;
p-4E-BP1, Cell signaling technology, catalog number: CST #2855;
p-AKT (Ser473), Cell signaling technology, catalog number: CST #9271;
p-AKT (Thr308), Cell signaling technology, catalog number: CST #13038;
p-GSK3b (Ser 9), Cell signaling technology, catalog number: CST#9322;
FASN, Cell signaling technology, catalog number: CST #3180;
ADIPSIN, R&D Systems, catalog number: # AF5430;
ADIPONECTIN, Thermo Fisher, catalog number: #PA1-054;
CEBPA, Santa cruz, catalog number: #sc-61);
HSP90, Proteintech, catalog number: #13171-1-AP;
GAPDH, Proteintech, catalog number: #HRP-60004;
Caveolin-1 (D46G3), Cell signaling technology, catalog number: CST, #3267;
Rabbit Alexa 488, Thermo Fisher Scientific, catalog number: # A27034;
F4/80, Cell signaling technology, catalog number: CST, #70076.
The dilution of antibodies were based on the recommendation on the manufacturer's website.

Validation

All antibodies were verified by the supplier. Validation statements are shown on the manufacturer's website.
1. p-mTOR antibody has been validated to be used for western blotting and mentioned species reactivity with mouse. (https://www.cellsignal.com/products/primary-antibodies/phospho-mtor-ser2448-antibody/2971)
2. p-S6K has been validated to be used for western blotting and mentioned species reactivity with mouse. (https://www.cellsignal.com/products/primary-antibodies/phospho-p70-s6-kinase-thr389-antibody/9205)
3. p-4E-BP1 antibody has been validated to be used for western blotting and mentioned species reactivity with mouse. (https://www.cellsignal.com/products/primary-antibodies/phospho-4e-bp1-thr37-46-236b4-rabbit-mab/2855)
4. p-AKT (S473) has been validated to be used for western blotting and mentioned species reactivity with mouse. (https://www.cellsignal.com/products/primary-antibodies/phospho-akt-ser473-antibody/9271)
5. p-AKT (T308) has been validated to be used for western blotting and mentioned species reactivity with mouse. (https://www.cellsignal.com/products/primary-antibodies/phospho-akt-thr308-d25e6-xp-rabbit-mab/13038)
6. p-GSK3b (Ser 9) has been validated to be used for western blotting and mentioned species reactivity with mouse. (https://www.cellsignal.com/products/primary-antibodies/phospho-gsk-3-beta-ser9-d3a4-rabbit-mab/9322)
7. FASN has been validated to be used for western blotting and mentioned species reactivity with mouse. (https://www.cellsignal.com/products/primary-antibodies/fatty-acid-synthase-c20g5-rabbit-mab/3180)

Eukaryotic cell lines

Policy information about cell lines and Sex and Gender in Research

Cell line source(s)	3T3-L1 and C3H10T1/2 were purchased from ATCC.
Authentication	None of the cell lines used were authenticated.
Mycoplasma contamination	Cell lines were not tested for mycoplasma contamination.
Commonly misidentified lines (See ICLAC register)	No commonly misidentified cell lines were used.

Animals and other research organisms

Policy information about studies involving animals; ARRIVE guidelines recommended for reporting animal research, and Sex and Gender in Research

Laboratory animals	6-17 week old male and female C57BL/6 mice were purchased from Jackson Laboratory. All mice were maintained in Columbia University animal facility with at 23 ± 1°C and a 12-hr light and dark cycle with ad libitum access to chow food (PicoLab Rodent 5053) and water.
Wild animals	The study did not involve wild animals.

Reporting on sex	The findings were reproduced in both male and female mice.
Field-collected samples	The study did not involve samples collected from the field.
Ethics oversight	The Columbia University Animal Care and Utilization Committee approved all animal studies.

Note that full information on the approval of the study protocol must also be provided in the manuscript.

Flow Cytometry

Plots

Confirm that:

☒ The axis labels state the marker and fluorochrome used (e.g. CD4-FITC).

☒ The axis scales are clearly visible. Include numbers along axes only for bottom left plot of group (a 'group' is an analysis of identical markers).

☒ All plots are contour plots with outliers or pseudocolor plots.

☒ A numerical value for number of cells or percentage (with statistics) is provided.

Methodology

Sample preparation	Cell cultures were treated as indicated and harvested by trypsinization. Cells were centrifuged (250 g, 5min) and resuspended in in appropriate amount of PBS containing 1% FBS to get concentration of 10^7 cells per 1 mL. Cells were filtered through the cell strainer right before the FACS analysis.
Instrument	BD influx equipped with 405, 488, 561 and 638nm lasers.
Software	FCS Express (7.14.0020) software
Cell population abundance	Cell sorting not employed.
Gating strategy	Using the FSC/SSC gating, debris was removed by gating on the main cell population. Gating strategy were provided in Extended Data Fig. 6e.

☒ Tick this box to confirm that a figure exemplifying the gating strategy is provided in the Supplementary Information.